Title: Preoptic Neurons that Regulate Hibernation Entry

Authors: Adrian J. Martinez[1,2]†, Christopher M. Reid[1]†, Aurora J. Lavin-Peter[1], Wenhui Li[1], Andrew S. Lee[1], Eric C. Griffith[3], Sinisa Hrvatin[1,4,5*]

Affiliations:

[1]Whitehead Institute for Biomedical Research, Cambridge, MA 02142, USA

[2]Department of Brain and Cognitive Sciences, Massachusetts Institute of Technology, Cambridge, MA 02142, USA

[3]Department of Neurobiology, Harvard Medical School, Boston, MA 02115, USA

[4]Department of Biology, Massachusetts Institute of Technology, Cambridge, MA 02142, USA

[5]Howard Hughes Medical Institute, Massachusetts Institute of Technology, Cambridge, MA, USA

*Corresponding author. Email shrvatin@wi.mit.edu (S.H.)

† These authors contributed equally to this work

Abstract: Seasonal hibernation allows species to survive harsh environments by entering a profound hypometabolic and hypothermic state called deep torpor (DT). However, the neural mechanisms controlling entry into this state remain poorly understood. Here, we map neuronal activity across hibernation stages in the Syrian hamster and identify DT-associated activity in the hypothalamic anterior preoptic area (aPOA) as essential for hibernation entry. Single-nucleus multiomic profiling enabled the design of a novel enhancer adeno-associated virus selectively targeting candidate glutamatergic neuronal subpopulations. Using this tool, we demonstrate that activity of a subpopulation of *Samd3*-positive glutamatergic neurons in the hamster aPOA is both necessary and sufficient for DT induction. Together, our findings identify a neuronal population regulating hibernation entry and provide the first genetic access to manipulate this complex behavior.

Main Text: The ability to maintain body temperature (T_b) within a narrow range is a defining feature of homeotherm physiology (*1*, *2*). However, to survive extreme environmental conditions, many mammals can initiate hypothermic and hypometabolic energy-conserving strategies such as hibernation or daily torpor (*3*–*8*). While T_b, heart rate, and metabolic rate decreases observed in daily torpor last only several hours (*9*, *10*), seasonal hibernation is characterized by deeper, repeated multi-day bouts of torpor periodically interrupted by arousals to euthermic T_b (*5*, *11*–*15*). Decades of study have characterized the homeostatic thermoregulatory circuitry that detects and responds to internal and external thermal cues (*1*, *2*, *16*–*27*). However, despite evidence that ambient and internal temperature (*3*), circadian clocks (*28*, *29*), adenosine, melatonin, and thyroid hormone signaling (*30*–*39*), and the peripheral nervous system (*40*) modulate hibernation dynamics, the neural mechanisms that initiate and sustain deep torpor (DT) in hibernating animals remain largely unexplored.

To probe the neural mechanisms that control entry into hibernation-associated deep torpor, we established a laboratory paradigm of hibernation in the Syrian hamster (*Mesocricetus auratus*), implanting each animal with telemetric temperature probes for continuous T_b monitoring. To induce hibernation, adult (5-6-week-old) animals housed at room temperature (~22ºC) with standard photoperiod (12 hours light (L): 12 hours dark (D)) were first shifted to a short photoperiod (8L:16D) for 8-10 weeks, followed by transfer to 4-5°C ambient temperature conditions to simulate seasonal changes (**Fig. 1A, B, Fig. S1A**). While this paradigm induced hibernation in both males and females, female hamsters were initially found to hibernate more readily (data not shown), with ~80%

51 initiating torpor bouts within six weeks of ambient temperature reduction. As a result, we
52 restricted our subsequent analyses to females.

53 While typical torpor-associated T_b decreases followed an exponential decay curve (n
54 = 1262 torpor bouts, **Fig. S1B**), animals exhibited some variability in torpor dynamics.
55 Altogether, 69% of animals (n = 271) achieved DT (minimal T_b = 5.5 ± 0.5°C, bout duration
56 60.3 ± 13.4 h) and 11% (n = 42) exhibited only shallow torpor bouts (minimal T_b = 12.2 ±
57 3.1°C, bout duration 6.8 ± 1.8 h), with 20% (n = 81) failing to initiate torpor during the 6-
58 week observation period (**Fig. 1C-F, Fig. S1C**). Periods of interbout euthermia (IBE)
59 between DT bouts lasted 15.3 ± 2.8 h (n = 2471 IBE periods, **Fig. 1E**). Moreover,
60 consistent with prior reports (*41*), torpor entry occurred preferentially during subjective
61 night (~ZT17-18) (n = 3,595 torpor bouts, **Fig. 1G**) and was characterized by a
62 stereotyped nesting behavior with curled posture and absence of gross motor movement,
63 food, or water intake (*5*, *15*). By contrast, arousal from DT exhibited no clear circadian
64 pattern (**Fig. 1H**), consonant with disrupted circadian clock oscillations at temperatures
65 below 15°C (*41*, *42*).

66

67 **POA activity regulates hamster entry into deep torpor**

68 Having established laboratory conditions for efficient hibernation induction, we
69 employed this system to investigate neural activity changes associated with DT onset. To
70 this end, we collected brain samples during DT and IBE, as well as from non-hibernating
71 control animals, and performed immunostaining for FOS, a marker of neuronal activity
72 (**Fig. 2A**). Given prior reports of neuronal activity marker induction in hypothalamic
73 regions during DT bouts (*41*, *43*, *44*), and classic studies showing that hypothalamic

74 lesions disrupt T_b regulation during hibernation (*45*), we focused our analysis primarily on
75 the hypothalamus. Among the 32 distinct regions analyzed, we observed DT-active
76 regions associated with circadian rhythm modulation (Suprachiasmatic nucleus) (*46–48*),
77 energy homeostasis (Arcuate nucleus) (*49–51*), and arousal (Paraventricular nucleus of
78 the thalamus) (*52*, *53*). Notably, the anteroventral periventricular nucleus (AVPe) within
79 the anterior POA exhibited the highest degree of FOS induction in DT relative to IBE or
80 non-hibernating control samples (14.1% vs. 6.9% and 0.8%, $P = 0.0685$ and $P < 0.001$,
81 respectively) (**Fig. 2B-D, Table S1, S2, Fig. S2A, B**).

82 To test directly whether hypothalamic neuronal activity is required for the initiation and
83 maintenance of hibernation, we stereotaxically injected adeno-associated virus (AAV)
84 expressing an inhibitory Gi-coupled DREADD (Designer Receptor Exclusively Activated
85 by Designer Drug; AAV-hSyn-hM4D(Gi)-mCherry) (*54*) into hibernating hamsters (**Fig.
86 2E**), systematically targeting different areas of the anterior hypothalamus that exhibited
87 substantial DT-associated activity. After allowing animals to recover and resume DT
88 bouts, we administered the DREADD agonist clozapine (CLZ) via drinking water. As
89 animals consumed CLZ during their IBE periods, we observed a cessation of torpor bouts
90 in a subset (4/13) of the tested animals, while all animals that underwent sham surgery
91 and received CLZ (5/5) readily re-entered torpor (**Fig. 2F-H, Fig. S2C**). Correlation of the
92 pattern of Gi-DREADD expression across animals with the degree of DT perturbation
93 identified subregions of the anterior POA (aPOA), including the medial preoptic area
94 (MPO), medial preoptic nucleus (MPN), and AVPe, as regions whose silencing was
95 associated with perturbed hibernation (**Fig. 2H-J, Table S3**). Together, these findings

implicate the anterior preoptic area as a key region whose activity is necessary for the initiation of DT bouts during hibernation.

Cross-species transcriptomic profiling identifies DT-active neuronal populations

The aPOA has been implicated in the regulation of fasting-induced daily torpor (FIT) in mice (*43*, *55–59*). Our chemogenetic silencing studies in hamster therefore raised the possibility that this region plays a conserved role in the control of hypometabolic states across mammals. To gain further insight into the diversity of neural cell types in the hamster POA and their relation to the cellular composition of the murine POA, we dissected and profiled the POA of 7 adult hamsters (4 females and 3 males) using single-nucleus paired RNA- and ATAC- sequencing (multiome) (**Fig. 3A**). We annotated the hamster POA cells by aligning and integrating the resulting data with recently published mouse POA multiome and spatial transcriptomic datasets (*60*, *61*), generating the first multiomic cross-species POA cellular taxonomy (**Fig. S3-5**).

Since activity of brain regions within the median and medial POA was essential for DT entry (**Fig. 2I**), we focused our analysis on these regions. Graph-based clustering identified major neuronal and non-neuronal cell classes, with further subclustering of neuronal cells (n = 26,761 cells) identifying 15 distinct GABAergic and 11 glutamatergic neuronal cell types shared between hamster and mouse (**Fig. 3B-D, Fig. S4**). Importantly, every neuronal cluster contained both mouse and hamster cells (**Fig. 3C**), and pair-wise transcriptional similarity analysis (cosine similarity score) between all hamster and murine neuronal cell clusters revealed consistent 1:1 cross-species relationships, further supporting the validity of our cross-species atlas alignment (**Fig. 3E**).

119 Moreover, with the exception of a few cell types, the relative cell type abundance across
120 POA neuronal clusters was largely preserved between hamster and mouse (**Fig. S5E)**.
121 Thus, our analyses reveal broad cellular homology between hamster and mouse POA.

122 Focusing more closely on POA neuronal populations implicated in FIT in the mouse,
123 we found that the expression patterns of molecular markers of mouse FIT-associated
124 neurons (*Slc17a6/Vglut2, Adcyap1, Esr1,* and *Ptger3*) were broadly conserved across
125 hamster and mouse POA cell types (**Fig. 3F, G**). Moreover, *in situ* hybridization (ISH)
126 analysis indicated that *Vglut2* and *Adcyap1*, two broad markers of FIT-regulating cells,
127 labeled neurons in similar anatomical locations in the mouse and hamster aPOA,
128 including the AVPe, MPO, and MnPO (animals = 4, **Fig. 3H, Fig. S6**). Leveraging these
129 findings, we carried out combined immunostaining and ISH on aPOA samples from
130 hamsters (n = 3) in deep torpor and found that the majority of DT-active (FOS-positive)
131 neurons express *Slc17a6/Vglut2* (65.2 ± 4.2%, animals = 3), with a considerable portion
132 expressing *Adcyap1* (34.0 ± 1.4%, animals = 3), and relatively few expressing
133 *Slc32a1/Vgat* (12.8 ± 1.5%, animals = 3, **Fig. 3I, J**, **Fig. S7A, B**). Together, these findings
134 suggest that homologous aPOA glutamatergic neuronal populations may be active during
135 mouse FIT and hamster DT.

136 To further test this idea, we leveraged anatomical information from our transcriptomic
137 and anatomical atlas to identify Glut-04, -06, -07, -09, -10, and -11 clusters as
138 corresponding to FIT-regulating neurons (hereafter collectively termed aPOA^{Vglut2}
139 neurons; **Fig. 3K, Fig. S7C**), and expression of the *Samd3* gene was found to exclusively
140 mark this population (**Fig. 3L**). Indeed, a substantial fraction of hamster DT-active (FOS+)
141 neurons also expressed *Samd3* (46.4 ± 4.1% of FOS+ AVPe neurons are positive for

142 *Samd3* mRNA, **Fig. 3M, N**), further supporting the idea that aPOA^{Vglut2} neurons are active
143 during DT entry and might regulate entry into this state. Together, our findings establish
144 the first cross-species atlas of the aPOA, a key region whose activity is necessary for the
145 initiation of DT bouts during hibernation, uncovering broad homology between mouse and
146 hamster cell types and implicating aPOA^{Vglut2} neurons as promising candidate drivers of
147 DT entry in the hamster.

148

149 **Enhancer-driven viral tools to access aPOA^{Vglut2} neurons**

150 To assess the functional role of aPOA^{Vglut2} neurons in hamster DT entry, we required
151 the ability to selectively target and manipulate these cell populations *in vivo*. Transgenic
152 options in the hamster remain limited, and a *CamkIIa* promoter-driven AAV exhibits poor
153 specificity for glutamatergic neurons in the hamster POA (42.6 ± 2.0%, animals = 4, **Fig.**
154 **S8**). Recently, AAV constructs incorporating compact cell-type-specific enhancer gene
155 regulatory elements (GREs) have offered a promising alternative to traditional transgenic
156 technologies in nonstandard species (*62–68*). We therefore sought to generate new
157 enhancer-AAV tools driving restricted payload expression in the target aPOA^{Vglut2} cell
158 population.

159 To develop a viral approach to selectively target aPOA^{Vglut2} neurons, we leveraged the
160 extensive murine single-nucleus chromatin accessibility (snATAC-seq) data included in
161 our multiomic cross-species atlas to identify conserved genomic elements exhibiting
162 selectively enhanced accessibility in aPOA^{Vglut2} neuron cell populations (**Fig. 4A**). First,
163 we employed a modeling-based approach to identify cell-type-specific nucleosome-
164 depleted gene regulatory regions. Subsequently, we performed differential accessibility

165 analysis to identify putative GREs with enriched accessibility in aPOA^{Vglut2} neuronal
166 populations relative to other neuronal subtypes **(Fig. 4B, Fig. S9)**, and filtered GREs
167 based on proximity to aPOA^{Vglut2} neuron-restricted marker genes (**Fig. 4C**). Notably, using
168 this approach, we identified a conserved 500 bp element proximal to the mouse *Samd3*
169 gene, hereafter termed *Samd3E*, that exhibited the highest accessibility enrichment in
170 aPOA^{Vglut2} neurons relative to caudal POA^{Vglut2} neurons and POA^{Vgat} neurons (FDR < 10^{-}
171 ^{300}, $\log_2$Fold Enrichment = 3.1, **Fig. 4B-E**), with similar aPOA^{Vglut2} neuron-enriched
172 accessibility also observed in the hamster (P = 10^{-173}, $\log_2$Fold Enrichment versus other
173 populations = 3.2, **Fig. 4F, Fig. S9**).

174 The resulting candidate mouse GRE sequences were synthesized and cloned into an
175 AAV backbone upstream of a minimal beta-globin promoter sequence and a red
176 fluorescent protein (RFP) reporter transgene prior to packaging into functional AAV8
177 particles for *in vivo* evaluation. Notably, the *Samd3E* element conferred remarkable
178 specificity, restricting reporter expression almost exclusively to *Vglut2*+ neurons in the
179 hamster aPOA (95.2 ± 1.2%; animals = 3), with substantial co-labeling of *Samd3*+ cells
180 (58.7 ± 3.2%, animals = 3, **Fig. 4G, H, Fig. S10**). Taken together, these findings highlight
181 the power of this approach to generate viral tools to study brain circuits across species,
182 including in hibernating animals, and establish the *Samd3E*-driven AAV (Samd3E-AAV)
183 as an effective tool for achieving targeted genetic access to glutamatergic neurons of the
184 anterior POA.

185

186 **aPOA^{Vglut2} neuronal activity is necessary and sufficient for deep torpor entry**

187 Employing our newly developed Samd3E-AAV, we set out to address the role of
188 aPOA^{Vglut2} neuronal activity in hibernation and DT by expressing an inhibitory Gi-
189 DREADD (AAV-Samd3E-hM4D(Gi)-EGFP) in hamster aPOA^{Vglut2} neurons (**Fig. 5A**).
190 Neuronal inhibition via CLZ administration had no significant effect on basal homeostatic
191 T_b or circadian T_b rhythmicity in control non-hibernating Gi-DREADD-expressing
192 hamsters (**Fig. S11A, B**). However, actively hibernating Gi-DREADD-expressing (n = 12)
193 animals showed a significant delay in the resumption of DT bouts following CLZ treatment
194 compared to when these same animals were administered a water-only vehicle control
195 (114.9 ± 45.4 hours vs. 64.1 ± 24.5 hours, P = 0.0003). Indeed, a majority (7/12) of CLZ-
196 treated Gi-DREADD-expressing animals failed to re-enter DT during the full 6-day course
197 of CLZ treatment, whereas none (0/12) of the animals failed to resume DT during
198 treatment with the vehicle control. Moreover, animals (n = 5) expressing a control reporter
199 payload (AAV-Samd3E-EGFP-Synaptophysin-mRuby) exhibited no significant difference
200 in the time to DT resumption following CLZ or vehicle treatment (61.6 ± 26.5 hours vs.
201 47.4 ± 10.2 hours, respectively. P = 0.6167), with all animals resuming torpor bouts within
202 the CLZ treatment window (**Fig. 5B, C**). Together, these results strongly suggest that
203 aPOA^{Vglut2} neuronal activity is required for entry into hibernation-associated DT.

204 To determine the extent to which aPOA^{Vglut2} neuron activity is sufficient to drive DT
205 entry, we selectively introduced an excitatory Gq-DREADD into hamster aPOA^{Vglut2}
206 neurons via our Samd3E-AAV (AAV-Samd3E-hM3D(Gq)-EGFP, **Fig. 5D**). CLZ
207 administration led to a rapid, significant drop in T_b in Gq-DREADD-expressing hamsters,
208 with the animals reaching a minimum body temperature of 13.9 ± 1.0ºC (P < 0.0001
209 relative to normothermia) and maintaining a reduced body temperature for 56.9 ± 13.1

210 hours, consistent with the induction of a prolonged torpor-like state (**Fig. 5E-G**). By
211 contrast, these same animals exhibited no discernable T_b change upon control PBS
212 administration (minimal T_b = 33.3 ± 2.4ºC, P = 0.8959 relative to normothermia). In
213 addition, CLZ treatment of Gq-DREADD-expressing animals (n = 6), but not PBS
214 treatment of the same animals (n = 6) or PBS/CLZ treatment of hamsters injected with a
215 control viral construct (n = 3), induced behaviors consonant with torpor entry, including a
216 curled posture and prolonged inactivity in the nest (P = 0.0168, **Fig. 5H, I, Fig. S12, Movie**
217 **S1**). Moreover, follow-up analyses revealed that the depth of CLZ-induced torpor across
218 animals correlated with levels of aPOA Gq-DREADD expression, suggesting that more
219 extensive $aPOA^{Vglut2}$ neuron activation drives deeper torpor-like bouts (r = -0.9577, P =
220 0.0104, **Fig. S11C, D**). Together, these findings show that $aPOA^{Vglut2}$ neuronal activity is
221 both necessary and sufficient to initiate a profound T_b decrease and DT-associated
222 nesting behaviors in the hamster.

223 Finally, given that $aPOA^{Vglut2}$ neurons are present in both the Syrian hamster (a
224 hibernator) and mouse (non-hibernator), we investigated whether virus-mediated
225 chemogenetic activation of this neuronal population in mice housed at low ambient
226 temperatures would drive a DT-like decrease in T_b. Indeed, CLZ treatment of Samd3E-
227 Gq-DREADD-transduced mice yielded a rapid and sustained drop in body temperature,
228 although markedly less than that observed in hamsters (**Fig. S13**). Thus, $aPOA^{Vglut2}$
229 neuronal activation is sufficient to elicit acute, pronounced reductions in core temperature
230 in both hibernating and non-hibernating species, with the difference in magnitude
231 suggestive of potential hibernator-specific evolutionary modifications in downstream
232 effector circuitry.

233

234 **Discussion**

235 Hibernation is a conserved, recurrently evolved energy-conserving strategy across
236 the mammalian lineage (*5*, *6*). Entry into this state is orchestrated by a complex interplay
237 of environmental cues and endocrine signals (*69*). However, despite prior reports of
238 hibernation-associated neural activity changes and classic lesion studies implicating the
239 POA (*41*, *43–45*), the specific neuronal populations regulating entry into hibernation-
240 associated deep torpor remained unknown. Here, using a Syrian hamster model, we
241 combine neural activity mapping with chemogenetic silencing to show that aPOA activity
242 is essential for deep torpor entry.

243 Our single-nucleus transcriptional and epigenomic profiling of the hamster POA
244 revealed strong cellular homology with the mouse, with no evidence of distinct cell
245 populations. Instead, we observed that aPOA glutamatergic neurons homologous to FIT-
246 regulating neuronal cell types in the mouse exhibit elevated activity upon hibernation-
247 associated DT in the hamster. Through the development and use of a novel enhancer-
248 driven AAV we show that aPOA^{Vglut2} neuron silencing blocks hibernation-associated DT
249 entry, whereas chemogenetic activation of this population drives a rapid fall in body
250 temperature and hibernation-like nesting behavior. Together, these studies establish
251 Samd3E-AAV-targeted aPOA^{Vglut2} neurons as key regulators of hibernation and provide
252 the first genetic access to hibernation-regulating circuits. Moreover, this Samd3E-AAV,
253 as well as the broader enhancer-driven viral targeting strategy, should be broadly
254 applicable to target these and related cell populations in other hibernating species.

255 Although mouse FIT and seasonal hibernation both involve profound reductions in T_b,
256 metabolic rate, and heart rate, these states differ markedly in their depth, duration, and
257 ethological significance. FIT represents a short-term response to food scarcity, lasting
258 only hours, whereas hibernation is typically a seasonal behavior involving deeper, multi-
259 day torpor bouts punctuated by brief periods of interbout euthermia. Our findings raise
260 the possibility that these differences reflect distinct connectivity and/or activity patterns of
261 $aPOA^{Vglut2}$ neurons in the two species, which might derive in part from remaining cross-
262 species gene expression differences observed in these cell types (**Fig. S7D**). Moreover,
263 chemogenetic activation of the $aPOA^{Vglut2}$ neurons in hamsters drives substantially
264 deeper torpor bouts than in mice, which might reflect limited efficiency in fully targeting
265 the $aPOA^{Vglut2}$ neuronal population (**Fig. S10**) or alternatively might indicate a requirement
266 for additional circuit elements for the full expression of deep torpor in the hamster.
267 Similarly, in the future it will be important to determine whether this $aPOA^{Vglut2}$ neuronal
268 population, or aspects of the broader hibernation-regulating circuitry, undergoes active
269 remodeling during the extended pre-hibernation conditioning period to support prolonged
270 bouts of deep torpor.

271 More broadly, our findings in hamster and mouse further support for the idea that
272 regulated heterothermy is an ancestral trait in mammals (*70*, *71*) and that core elements
273 of the underlying torpor circuitry may be broadly conserved—potentially not only across
274 torpid and hibernating mammals, but also in species that do not naturally exhibit these
275 states. Indeed, *in situ* hybridization data from the marmoset (*Callithrix jacchus*), a non-
276 hibernating primate, indicate that neurons expressing deep torpor-associated markers
277 are present in the homologous regions within the aPOA (**Fig. S14**) (*72*–*74*). Our study

thus lays a foundation for future efforts to define broader hibernation-regulating circuitry, including upstream inputs conveying seasonal cues, downstream pathways mediating systemic adaptations, and the cellular mechanisms that allow neurons to function at near-freezing temperatures. Beyond advancing basic understanding of hibernation, these insights may eventually inform approaches to harness the mechanisms behind this amazing adaption to advance medicine in areas such as therapeutic hypothermia, organ preservation, central metabolic control, suppression of muscle atrophy, and aging.

References

1. C. L. Tan, Z. A. Knight, Regulation of Body Temperature by the Nervous System. *Neuron* **98**, 31–48 (2018).

2. S. F. Morrison, K. Nakamura, Central Mechanisms for Thermoregulation. *Annu. Rev. Physiol.* **81**, 285–308 (2019).

3. H. C. Heller, H. T. Hammel, CNS control of body temperature during hibernation. *Comp. Biochem. Physiol. A Physiol.* **41**, 349–359 (1972).

4. G. A. Sunagawa, M. Takahashi, Hypometabolism during Daily Torpor in Mice is Dominated by Reduction in the Sensitivity of the Thermoregulatory System. *Sci. Rep.* **6**, 1–14 (2016).

5. F. Geiser, Metabolic Rate and Body Temperature Reduction During Hibernation and Daily Torpor. *Annu. Rev. Physiol.* **66**, 239–274 (2004).

6. F. Geiser, *Ecological Physiology of Daily Torpor and Hibernation* (Springer, Cham, Switzerland, 2021).

7. K. L. Drew, C. L. Buck, B. M. Barnes, S. L. Christian, B. T. Rasley, M. B. Harris, Central nervous system regulation of mammalian hibernation: implications for metabolic suppression and ischemia tolerance. *J Neurochem* **102**, 1713–1726 (2007).

8. H. C. Heller, Hibernation: neural aspects. *Annu. Rev. Physiol.* **41**, 305–321 (1979).

9. S. R. Morton, Torpor and Nest-Sharing in Free-Living Sminthopsis crassicaudata (Marsupialia) and Mus musculus (Rodentia). *J. Mammal.* **59**, 569–575 (1978).

10. S. J. Swoap, M. J. Gutilla, Cardiovascular changes during daily torpor in the laboratory mouse. *Am. J. Physiol.-Regul. Integr. Comp. Physiol.* **297**, R769–R774 (2009).

11. B. M. Barnes, Freeze avoidance in a mammal: body temperatures below 0 degree C in an Arctic hibernator. *Science* **244**, 1593–1595 (1989).

12. G. Heldmaier, S. Ortmann, R. Elvert, Natural hypometabolism during hibernation and daily torpor in mammals. *Respir. Physiol. Neurobiol.* **141**, 317–329 (2004).

13. F. G. Revel, A. Herwig, M.-L. Garidou, H. Dardente, J. S. Menet, M. Masson-Pévet, V. Simonneaux, M. Saboureau, P. Pévet, The circadian clock stops ticking during deep hibernation in the European hamster. *Proc. Natl. Acad. Sci.* **104**, 13816–13820 (2007).

318 14. S. M. Mohr, S. N. Bagriantsev, E. O. Gracheva, Cellular, Molecular, and
319 Physiological Adaptations of Hibernation: The Solution to Environmental
320 Challenges. *Annu. Rev. Cell Dev. Biol.* **36**, 315–338 (2020).

321 15. Y. Chayama, L. Ando, Y. Tamura, M. Miura, Y. Yamaguchi, Decreases in body
322 temperature and body mass constitute pre-hibernation remodelling in the Syrian
323 golden hamster, a facultative mammalian hibernator. *R. Soc. Open Sci.* **3**, 160002
324 (2016).

325 16. R. S. Teague, S. W. Ranson, The role of the anterior hypothalamus in
326 temperature regulation. *Am. J. Physiol.-Leg. Content* **117**, 562–570 (1936).

327 17. H. T. Hammel, J. B. Pierce, Regulation of Internal Body Temperature. *Annu. Rev.*
328 *Physiol.* **30**, 641–710 (1968).

329 18. M. V. Zaretskaia, D. V. Zaretsky, A. Shekhar, J. A. DiMicco, Chemical stimulation
330 of the dorsomedial hypothalamus evokes non-shivering thermogenesis in
331 anesthetized rats. *Brain Res.* **928**, 113–125 (2002).

332 19. K. Nakamura, S. F. Morrison, A thermosensory pathway that controls body
333 temperature. *Nat Neurosci* **11**, 62–71 (2008).

334 20. H. Hensel, Neural processes in thermoregulation. *Physiol. Rev.* **53**, 948–1017
335 (1973).

336 21. C. Jessen, Thermal afferents in the control of body temperature. *Pharmacol.*
337 *Ther.* **28**, 107–134 (1985).

338 22. H. T. Hammel, J. D. Hardy, M. M. Fusco, Thermoregulatory responses to
339 hypothalamic cooling in unanesthetized dogs. *Am J Physiol* **198**, 481–6 (1960).

340 23. H. W. Magoun, F. Harrison, J. R. Brobeck, S. W. Ranson, Activation of heat loss
341 mechanisms by local heating of the brain. *J. Neurophysiol.* **1**, 101–114 (1938).

342 24. C. L. Tan, E. K. Cooke, D. E. Leib, Y.-C. Lin, G. E. Daly, C. A. Zimmerman, Z. A.
343 Knight, Warm-Sensitive Neurons that Control Body Temperature. *Cell* **167**, 47-
344 59.e15 (2016).

345 25. K. Song, H. Wang, G. B. Kamm, J. Pohle, F. de C. Reis, P. Heppenstall, H.
346 Wende, J. Siemens, The TRPM2 channel is a hypothalamic heat sensor that limits
347 fever and can drive hypothermia. *Science* **353**, 1393–1398 (2016).

348 26. S. Yu, E. Qualls-Creekmore, K. Rezai-Zadeh, Y. Jiang, H. R. Berthoud, C. D.
349 Morrison, A. V. Derbenev, A. Zsombok, H. Munzberg, Glutamatergic Preoptic Area
350 Neurons That Express Leptin Receptors Drive Temperature-Dependent Body
351 Weight Homeostasis. *J Neurosci* **36**, 5034–46 (2016).

352 27. Q. Zhou, X. Fu, J. Xu, S. Dong, C. Liu, D. Cheng, C. Gao, M. Huang, Z. Liu, X.
353 Ni, R. Hua, H. Tu, H. Sun, Q. Shen, B. Chen, J. Zhang, L. Zhang, H. Yang, J. Hu,
354 W. Yang, W. Pei, Q. Yao, X. Sheng, J. Zhang, W. Z. Yang, W. L. Shen,
355 Hypothalamic warm-sensitive neurons require TRPC4 channel for detecting internal
356 warmth and regulating body temperature in mice. *Neuron* **111**, 387-404 e8 (2023).

357 28. P. M. Vitale, J. M. Darrow, M. J. Duncan, C. A. Shustak, B. D. Goldman, Effects
358 of photoperiod, pinealectomy and castration on body weight and daily torpor in
359 Djungarian hamsters (Phodopus sungorus). *J. Endocrinol.* **106**, 367–375 (1985).

360 29. M. J. Paul, A. S. Kauffman, I. Zucker, Feeding schedule controls circadian timing
361 of daily torpor in SCN-ablated Siberian hamsters. *J. Biol. Rhythms* **19**, 226–237
362 (2004).

363 30. A. M. Magariños, B. S. McEwen, M. Saboureau, P. Pevet, Rapid and reversible
364 changes in intrahippocampal connectivity during the course of hibernation in
365 European hamsters. *Proc. Natl. Acad. Sci. U. S. A.* **103**, 18775–18780 (2006).

366 31. T. Korhonen, A.-M. Mustonen, P. Nieminen, S. Saarela, Effects of cold exposure,
367 exogenous melatonin and short-day treatment on the weight-regulation and body
368 temperature of the Siberian hamster (Phodopus sungorus). *Regul. Pept.* **149**, 60–66
369 (2008).

370 32. T. L. Stanton, J. C. Daley, S. K. Salzman, Prolongation of hibernation bout
371 duration by continuous intracerebroventricular infusion of melatonin in hibernating
372 ground squirrels. *Brain Res.* **413**, 350–355 (1987).

373 33. H. E. Chmura, C. Duncan, B. Saer, J. T. Moore, B. M. Barnes, C. Loren Buck, H.
374 C. Christian, A. S. I. Loudon, C. T. Williams, Hypothalamic remodeling of thyroid
375 hormone signaling during hibernation in the arctic ground squirrel. *Commun. Biol.* **5**,
376 492 (2022).

377 34. Y. Tamura, M. Shintani, A. Nakamura, M. Monden, H. Shiomi, Phase-specific
378 central regulatory systems of hibernation in Syrian hamsters. *Brain Res.* **1045**, 88–
379 96 (2005).

380 35. J. M. Olson, T. R. Jinka, L. K. Larson, J. J. Danielson, J. T. Moore, J. Carpluck,
381 K. L. Drew, Circannual rhythm in body temperature, torpor, and sensitivity to A_1
382 adenosine receptor agonist in arctic ground squirrels. *J. Biol. Rhythms* **28**, 201–207
383 (2013).

384 36. T. R. Jinka, Ø. Tøien, K. L. Drew, Season primes the brain in an arctic hibernator
385 to facilitate entrance into torpor mediated by adenosine A(1) receptors. *J. Neurosci.*
386 *Off. J. Soc. Neurosci.* **31**, 10752–10758 (2011).

387 37. C. Frare, M. E. Jenkins, S. J. Soldin, K. L. Drew, The Raphe Pallidus and the
388 Hypothalamic-Pituitary-Thyroid Axis Gate Seasonal Changes in Thermoregulation in

389 the Hibernating Arctic Ground Squirrel (Urocitellus parryii). *Front. Physiol.* **9**, 1747
390 (2018).

391 38. T. L. Stanton, A. Winokur, A. L. Beckman, Seasonal variation in thyrotropin-
392 releasing hormone (TRH) content of different brain regions and the pineal in the
393 mammalian hibernator, Citellus lateralis. *Regul. Pept.* **3**, 135–144 (1982).

394 39. S. M. Mohr, R. Dai Pra, M. P. Platt, V. V. Feketa, M. Shanabrough, L. Varela, A.
395 Kristant, H. Cao, D. K. Merriman, T. L. Horvath, S. N. Bagriantsev, E. O. Gracheva,
396 Hypothalamic hormone deficiency enables physiological anorexia in ground
397 squirrels during hibernation. *Nat. Commun.* **15**, 5803 (2024).

398 40. M. B. Harris, W. K. Milsom, Parasympathetic influence on heart rate in euthermic
399 and hibernating ground squirrels. *J. Exp. Biol.* **198**, 931–937 (1995).

400 41. F. A. F. Markussen, F. Cazarez-Marquez, V. J. Melum, D. G. Hazlerigg, S. H.
401 Wood, c-fos induction in the choroid plexus, tanycytes and pars tuberalis is an early
402 indicator of spontaneous arousal from torpor in a deep hibernator. *J Exp Biol* **227**
403 (2024).

404 42. R. Enoki, N. Kon, K. Shimizu, K. Kobayashi, S. Hiro, C.-P. Chang, T. Nakane, H.
405 Ishii, J. Sakamoto, Y. Yamaguchi, T. Nemoto, Cold-induced suspension and
406 resetting of Ca2+ and transcriptional rhythms in the suprachiasmatic nucleus
407 neurons. *iScience* **26**, 108390 (2023).

408 43. M. Cheng, M. Wang, L. Wang, F. Yin, J. Shen, X. Xing, Y. Shi, Z. Liu, P. Wu, W.
409 Gao, Y. Fan, P. Cao, C. Zhan, Brainstem catecholaminergic neurons induce torpor
410 during fasting by orchestrating cardiovascular and thermoregulation changes. *Nat.*
411 *Commun.* **16**, 5954 (2025).

412 44. A. Bratincsak, D. McMullen, S. Miyake, Z. E. Toth, J. M. Hallenbeck, M.
413 Palkovits, Spatial and temporal activation of brain regions in hibernation: c-fos
414 expression during the hibernation bout in thirteen-lined ground squirrel. *J Comp*
415 *Neurol* **505**, 443–58 (2007).

416 45. D. J. Weidler, A. M. Earle, G. G. Myers, G. C. Sieck, Effect of hypothalamic
417 lesions on temperature regulation in hibernating ground squirrels. *Brain Res.* **65**,
418 175–179 (1974).

419 46. M. H. Hastings, E. S. Maywood, M. Brancaccio, Generation of circadian rhythms
420 in the suprachiasmatic nucleus. *Nat. Rev. Neurosci.* **19**, 453–469 (2018).

421 47. D. K. Welsh, J. S. Takahashi, S. A. Kay, Suprachiasmatic Nucleus: Cell
422 Autonomy and Network Properties. *Annu. Rev. Physiol.* **72**, 551–577 (2010).

423 48. D. R. Weaver, The Suprachiasmatic Nucleus: A 25-Year Retrospective. *J. Biol.*
424 *Rhythms* **13**, 100–112 (1998).

49. M. L. Andermann, B. B. Lowell, Toward a Wiring Diagram Understanding of Appetite Control. *Neuron* **95**, 757–778 (2017).

50. R. D. Cone, M. A. Cowley, A. A. Butler, W. Fan, D. L. Marks, M. J. Low, The arcuate nucleus as a conduit for diverse signals relevant to energy homeostasis. *Int. J. Obes.* **25**, S63–S67 (2001).

51. A. Jais, J. C. Brüning, Arcuate Nucleus-Dependent Regulation of Metabolism—Pathways to Obesity and Diabetes Mellitus. *Endocr. Rev.* **43**, 314–328 (2022).

52. Y. D. Van der Werf, M. P. Witter, H. J. Groenewegen, The intralaminar and midline nuclei of the thalamus. Anatomical and functional evidence for participation in processes of arousal and awareness. *Brain Res. Rev.* **39**, 107–140 (2002).

53. B. E. Jones, Arousal systems. *Front. Biosci. J. Virtual Libr.* **8**, s438-451 (2003).

54. B. L. Roth, DREADDs for Neuroscientists. *Neuron* **89**, 683–694 (2016).

55. S. Hrvatin, S. Sun, O. F. Wilcox, H. Yao, A. J. Lavin-Peter, M. Cicconet, E. G. Assad, M. E. Palmer, S. Aronson, A. S. Banks, E. C. Griffith, M. E. Greenberg, Neurons that regulate mouse torpor. *Nature* **583**, 115–121 (2020).

56. T. M. Takahashi, G. A. Sunagawa, S. Soya, M. Abe, K. Sakurai, K. Ishikawa, M. Yanagisawa, H. Hama, E. Hasegawa, A. Miyawaki, K. Sakimura, M. Takahashi, T. Sakurai, A discrete neuronal circuit induces a hibernation-like state in rodents. *Nature* **583**, 109–114 (2020).

57. Z. Zhang, F. M. C. V. Reis, Y. He, J. W. Park, J. R. DiVittorio, N. Sivakumar, J. E. van Veen, S. Maesta-Pereira, M. Shum, I. Nichols, M. G. Massa, S. Anderson, K. Paul, M. Liesa, O. A. Ajijola, Y. Xu, A. Adhikari, S. M. Correa, Estrogen-sensitive medial preoptic area neurons coordinate torpor in mice. *Nat. Commun.* **11**, 6378 (2020).

58. N. L. S. Machado, N. Lynch, L. H. A. Costa, D. Melville, H. Kucukdereli, S. Kaur, A. S. Banks, F. Raffin, O. D. Ramirez-Plascencia, S. Aten, J. D. Lima, S. S. Bandaru, R. D. Palmiter, C. B. Saper, Preoptic EP3R neurons constitute a two-way switch for fever and torpor. *Nature*, 1–10 (2025).

59. M. Ambler, T. Hitrec, A. Wilson, M. Cerri, A. Pickering, Neurons in the Dorsomedial Hypothalamus Promote, Prolong, and Deepen Torpor in the Mouse. *J. Neurosci. Off. J. Soc. Neurosci.* **42**, 4267–4277 (2022).

60. H. S. Kaplan, B. L. Logeman, K. Zhang, T. A. Yawitz, C. Santiago, N. Sohail, M. Talay, C. Seo, S. Naumenko, S. J. Ho Sui, D. D. Ginty, B. Ren, C. Dulac, Sensory input, sex and function shape hypothalamic cell type development. *Nature*, doi: 10.1038/s41586-025-08603-0 (2025).

460 61. M. Zhang, X. Pan, W. Jung, A. R. Halpern, S. W. Eichhorn, Z. Lei, L. Cohen, K.
461 A. Smith, B. Tasic, Z. Yao, H. Zeng, X. Zhuang, Molecularly defined and spatially
462 resolved cell atlas of the whole mouse brain. *Nature* **624**, 343–354 (2023).

463 62. J. Dimidschstein, Q. Chen, R. Tremblay, S. L. Rogers, G.-A. Saldi, L. Guo, Q.
464 Xu, R. Liu, C. Lu, J. Chu, J. S. Grimley, A.-R. Krostag, A. Kaykas, M. C. Avery, M. S.
465 Rashid, M. Baek, A. L. Jacob, G. B. Smith, D. E. Wilson, G. Kosche, I. Kruglikov, T.
466 Rusielewicz, V. C. Kotak, T. M. Mowery, S. A. Anderson, E. M. Callaway, J. S.
467 Dasen, D. Fitzpatrick, V. Fossati, M. A. Long, S. Noggle, J. H. Reynolds, D. H.
468 Sanes, B. Rudy, G. Feng, G. Fishell, A viral strategy for targeting and manipulating
469 interneurons across vertebrate species. *Nat. Neurosci.* **19**, 1743–1749 (2016).

470 63. T. Cronin, L. H. Vandenberghe, P. Hantz, J. Juttner, A. Reimann, Á. Kacsó, R. M.
471 Huckfeldt, V. Busskamp, H. Kohler, P. S. Lagali, B. Roska, J. Bennett, Efficient
472 transduction and optogenetic stimulation of retinal bipolar cells by a synthetic adeno-
473 associated virus capsid and promoter. *EMBO Mol. Med.* **6**, 1175–1190 (2014).

474 64. Y. Ben-Simon, M. Hooper, S. Narayan, T. L. Daigle, D. Dwivedi, S. W. Way, A.
475 Oster, D. A. Stafford, J. K. Mich, M. J. Taormina, R. A. Martinez, X. Opitz-Araya, J.
476 R. Roth, J. R. Alexander, S. Allen, A. Amster, J. Arbuckle, A. Ayala, P. M. Baker, T.
477 E. Bakken, T. Barcelli, S. Barta, J. Bendrick, D. Bertagnolli, C. Bielstein, P.
478 Bishwakarma, J. Bowlus, G. Boyer, K. Brouner, B. Casian, T. Casper, A. B. Chakka,
479 R. Chakrabarty, R. K. Chance, S. Chavan, M. Clark, K. Colbert, F. Collman, S.
480 Daniel, M. Departee, P. DiValentin, N. Donadio, N. Dotson, T. Egdorf, T. Fliss, M.
481 Gabitto, J. Garcia, A. Gary, M. Gasperini, J. Gloe, J. Goldy, B. B. Gore, L. Graybuck,
482 N. Greisman, F. Haeseleer, C. Halterman, Z. Haradon, S. D. Hastings, O. Helback,
483 W. Ho, D. Hockemeyer, C. Huang, S. Huff, A. Hunker, N. Johansen, D. Jones, Z.
484 Juneau, B. Kalmbach, M. Kannan, S. Khem, E. Kussick, R. Kutsal, R. Larsen, C.
485 Lee, A. Y. Lee, M. Leibly, G. H. Lenz, S. Li, E. Liang, N. Lusk, Z. Madigan, J. Malloy,
486 J. Malone, R. McCue, J. Melchor, T. Mollenkopf, S. Moosman, E. Morin, D.
487 Newman, L. Ng, K. Ngo, V. Omstead, S. Otto, A. Oyama, N. Pena, T. Pham, E.
488 Phillips, C. A. Pom, L. Potekhina, S. Ransford, P. L. Ray, D. Rette, C. Reynoldson,
489 C. Rimorin, D. Rocha, A. Ruiz, R. E. A. Sanchez, L. Sawyer, A. Sedeno-Cortes, J.
490 P. Sevigny, N. Shapovalova, N. Shepard, L. Shulga, A. R. Sigler, L. Siverts, S.
491 Soliman, S. Somasundaram, B. Staats, K. Stewart, E. Szelenyi, M. Tieu, C. Trader,
492 A. Tran, C. T. J. van Velthoven, M. Walker, Y. Wang, N. Weed, M. Wirthlin, T.
493 Wood, B. Wynalda, Z. Yao, T. Zhou, J. Ariza, N. Dee, M. Reding, K. Ronellenfitch,
494 S. Mufti, S. M. Sunkin, K. A. Smith, L. Esposito, J. Waters, B. Thyagarajan, S. Yao,
495 E. S. Lein, H. Zeng, B. P. Levi, J. Ngai, J. T. Ting, B. Tasic, A suite of enhancer
496 AAVs and transgenic mouse lines for genetic access to cortical cell types. *Cell* **188**,
497 3045-3064 e23 (2025).

498 65. L. T. Graybuck, T. L. Daigle, A. E. Sedeño-Cortés, M. Walker, B. Kalmbach, G.
499 H. Lenz, E. Morin, T. N. Nguyen, E. Garren, J. L. Bendrick, T. K. Kim, T. Zhou, M.
500 Mortrud, S. Yao, L. A. Siverts, R. Larsen, B. B. Gore, E. R. Szelenyi, C. Trader, P.
501 Balaram, C. T. J. van Velthoven, M. Chiang, J. K. Mich, N. Dee, J. Goldy, A. H.
502 Cetin, K. Smith, S. W. Way, L. Esposito, Z. Yao, V. Gradinaru, S. M. Sunkin, E. Lein,

503 B. P. Levi, J. T. Ting, H. Zeng, B. Tasic, Enhancer viruses for combinatorial cell-
504 subclass-specific labeling. *Neuron* **109**, 1449-1464.e13 (2021).

505 66. S. Hrvatin, C. P. Tzeng, M. A. Nagy, H. Stroud, C. Koutsioumpa, O. F. Wilcox, E.
506 G. Assad, J. Green, C. D. Harvey, E. C. Griffith, M. E. Greenberg, A scalable
507 platform for the development of cell-type-specific viral drivers. *eLife* **8**, e48089
508 (2019).

509 67. M. A. Nagy, S. Price, K. Wang, S. Gill, E. Ren, L. Jayne, V. Pajak, S. Deighan, B.
510 Liu, X. Lu, A. Diallo, S.-C. Lo, R. Kleiman, C. Henderson, J. Suh, E. C. Griffith, M. E.
511 Greenberg, S. Hrvatin, Cis-regulatory elements driving motor neuron-selective viral
512 payload expression within the mammalian spinal cord. *Proc. Natl. Acad. Sci.* **121**,
513 e2418024121 (2024).

514 68. A. C. Hunker, M. E. Wirthlin, G. Gill, N. J. Johansen, M. Hooper, V. Omstead, S.
515 Vargas, M. N. Lerma, N. Taskin, N. Weed, W. D. Laird, Y. M. Bishaw, J. L. Bendrick,
516 B. B. Gore, Y. Ben-Simon, X. Opitz-Araya, R. A. Martinez, S. W. Way, B.
517 Thyagarajan, S. Otto, R. E. A. Sanchez, J. R. Alexander, A. Amaya, A. Amster, J.
518 Arbuckle, A. Ayala, P. M. Baker, T. Barcelli, S. Barta, D. Bertagnolli, C. Bielstein, P.
519 Bishwakarma, J. Bowlus, G. Boyer, K. Brouner, B. Casian, T. Casper, A. B. Chakka,
520 R. Chakrabarty, P. Chong, M. Clark, K. Colbert, S. Daniel, T. Dawe, M. Departee, P.
521 DiValentin, N. P. Donadio, N. I. Dotson, D. Dwivedi, T. Egdorf, T. Fliss, A. Gary, J.
522 Goldy, C. Grasso, E. L. Groce, K. Gudsnuk, W. Han, Z. Haradon, S. Hastings, O.
523 Helback, W. V. Ho, C. Huang, T. Johnson, D. L. Jones, Z. Juneau, J. Kenney, M.
524 Leibly, S. Li, E. Liang, H. Loeffler, N. A. Lusk, Z. Madigan, J. Malloy, J. Malone, R.
525 McCue, J. Melchor, J. K. Mich, S. Moosman, E. Morin, R. Naidoo, D. Newman, K.
526 Ngo, K. Nguyen, A. L. Oster, B. Ouellette, A. A. Oyama, N. Pena, T. Pham, E.
527 Phillips, C. Pom, L. Potekhina, S. Ransford, P. L. Ray, M. Reding, D. F. Rette, C.
528 Reynoldson, C. Rimorin, A. R. Sigler, D. B. Rocha, K. Ronellenfitch, A. Ruiz, L.
529 Sawyer, J. P. Sevigny, N. V. Shapovalova, N. Shepard, L. Shulga, S. Soliman, B.
530 Staats, M. J. Taormina, M. Tieu, Y. Wang, J. Wilkes, T. Wood, T. Zhou, A. Williford,
531 N. Dee, T. Mollenkopf, L. Ng, L. Esposito, B. E. Kalmbach, S. Yao, J. Ariza, F.
532 Collman, S. Mufti, K. Smith, J. Waters, I. Ersing, M. Patrick, H. Zeng, E. S. Lein, Y.
533 Kojima, G. Horwitz, S. F. Owen, B. P. Levi, T. L. Daigle, B. Tasic, T. E. Bakken, J. T.
534 Ting, Enhancer AAV toolbox for accessing and perturbing striatal cell types and
535 circuits. *Neuron* **113**, 1507-1524 e17 (2025).

536 69. M. S. Junkins, S. N. Bagriantsev, E. O. Gracheva, Towards understanding the
537 neural origins of hibernation. *J. Exp. Biol.* **225**, jeb229542 (2022).

538 70. B. G. Lovegrove, A phenology of the evolution of endothermy in birds and
539 mammals. *Biol Rev Camb Philos Soc* **92**, 1213–1240 (2017).

540 71. F. Geiser, C. Stawski, C. B. Wacker, J. Nowack, Phoenix from the Ashes: Fire,
541 Torpor, and the Evolution of Mammalian Endothermy. *Front Physiol* **8**, 842 (2017).

72. Y. Kita, H. Nishibe, Y. Wang, T. Hashikawa, S. S. Kikuchi, M. U, A. C. Yoshida, C. Yoshida, T. Kawase, S. Ishii, H. Skibbe, T. Shimogori, Cellular-resolution gene expression profiling in the neonatal marmoset brain reveals dynamic species- and region-specific differences. *Proc. Natl. Acad. Sci.* **118**, e2020125118 (2021).

73. T. Shimogori, A. Abe, Y. Go, T. Hashikawa, N. Kishi, S. S. Kikuchi, Y. Kita, K. Niimi, H. Nishibe, M. Okuno, K. Saga, M. Sakurai, M. Sato, T. Serizawa, S. Suzuki, E. Takahashi, M. Tanaka, S. Tatsumoto, M. Toki, M. U, Y. Wang, K. J. Windak, H. Yamagishi, K. Yamashita, T. Yoda, A. C. Yoshida, C. Yoshida, T. Yoshimoto, H. Okano, Digital gene atlas of neonate common marmoset brain. *Neurosci. Res.* **128**, 1–13 (2018).

74. Gene Structural Search | Marmoset Gene Atlas. https://gene-atlas.brainminds.jp/gene-structural/.

75. E. S. Lein, M. J. Hawrylycz, N. Ao, M. Ayres, A. Bensinger, A. Bernard, A. F. Boe, M. S. Boguski, K. S. Brockway, E. J. Byrnes, L. Chen, L. Chen, T.-M. Chen, M. C. Chin, J. Chong, B. E. Crook, A. Czaplinska, C. N. Dang, S. Datta, N. R. Dee, A. L. Desaki, T. Desta, E. Diep, T. A. Dolbeare, M. J. Donelan, H.-W. Dong, J. G. Dougherty, B. J. Duncan, A. J. Ebbert, G. Eichele, L. K. Estin, C. Faber, B. A. Facer, R. Fields, S. R. Fischer, T. P. Fliss, C. Frensley, S. N. Gates, K. J. Glattfelder, K. R. Halverson, M. R. Hart, J. G. Hohmann, M. P. Howell, D. P. Jeung, R. A. Johnson, P. T. Karr, R. Kawal, J. M. Kidney, R. H. Knapik, C. L. Kuan, J. H. Lake, A. R. Laramee, K. D. Larsen, C. Lau, T. A. Lemon, A. J. Liang, Y. Liu, L. T. Luong, J. Michaels, J. J. Morgan, R. J. Morgan, M. T. Mortrud, N. F. Mosqueda, L. L. Ng, R. Ng, G. J. Orta, C. C. Overly, T. H. Pak, S. E. Parry, S. D. Pathak, O. C. Pearson, R. B. Puchalski, Z. L. Riley, H. R. Rockett, S. A. Rowland, J. J. Royall, M. J. Ruiz, N. R. Sarno, K. Schaffnit, N. V. Shapovalova, T. Sivisay, C. R. Slaughterbeck, S. C. Smith, K. A. Smith, B. I. Smith, A. J. Sodt, N. N. Stewart, K.-R. Stumpf, S. M. Sunkin, M. Sutram, A. Tam, C. D. Teemer, C. Thaller, C. L. Thompson, L. R. Varnam, A. Visel, R. M. Whitlock, P. E. Wohnoutka, C. K. Wolkey, V. Y. Wong, M. Wood, M. B. Yaylaoglu, R. C. Young, B. L. Youngstrom, X. F. Yuan, B. Zhang, T. A. Zwingman, A. R. Jones, Genome-wide atlas of gene expression in the adult mouse brain. *Nature* **445**, 168–176 (2007).

76. M. Trefna, M. Goris, C. M. C. Thissen, V. A. Reitsema, J. J. Bruintjes, E. L. de Vrij, H. R. Bouma, A. S. Boerema, R. H. Henning, The influence of sex and diet on the characteristics of hibernation in Syrian hamsters. *J. Comp. Physiol. [B]* **187**, 725–734 (2017).

77. M. Negrini, G. Wang, A. Heuer, T. Björklund, M. Davidsson, AAV Production Everywhere: A Simple, Fast, and Reliable Protocol for In-house AAV Vector Production Based on Chloroform Extraction. *Curr. Protoc. Neurosci.* **93**, e103 (2020).

78. R. I. Wood, L. P. Morin, *A Stereotaxic Atlas of the Golden Hamster Brain* (Elsevier Science, 2001).

583 79. R. Lopez, J. Regier, M. B. Cole, M. I. Jordan, N. Yosef, Deep generative
584 modeling for single-cell transcriptomics. *Nat. Methods* **15**, 1053–1058 (2018).

585 80. F. A. Wolf, P. Angerer, F. J. Theis, SCANPY: large-scale single-cell gene
586 expression data analysis. *Genome Biol.* **19**, 15 (2018).

587 81. C. Xu, R. Lopez, E. Mehlman, J. Regier, M. I. Jordan, N. Yosef, Probabilistic
588 harmonization and annotation of single-cell transcriptomics data with deep
589 generative models. *Mol. Syst. Biol.* **17**, e9620 (2021).

590 82. C. Bravo González-Blas, L. Minnoye, D. Papasokrati, S. Aibar, G. Hulselmans, V.
591 Christiaens, K. Davie, J. Wouters, S. Aerts, cisTopic: cis-regulatory topic modeling
592 on single-cell ATAC-seq data. *Nat. Methods* **16**, 397–400 (2019).

593 83. P. Bankhead, M. B. Loughrey, J. A. Fernández, Y. Dombrowski, D. G. McArt, P.
594 D. Dunne, S. McQuaid, R. T. Gray, L. J. Murray, H. G. Coleman, J. A. James, M.
595 Salto-Tellez, P. W. Hamilton, QuPath: Open source software for digital pathology
596 image analysis. *Sci. Rep.* **7**, 16878 (2017).

597 84. T. Goldsborough, A. O'Callaghan, F. Inglis, L. Leplat, A. Filby, H. Bilen, P.
598 Bankhead, A novel channel invariant architecture for the segmentation of cells and
599 nuclei in multiplexed images using InstanSeg. bioRxiv [Preprint] (2024).
600 https://doi.org/10.1101/2024.09.04.611150.

601 85. O. Friard, M. Gamba, BORIS: a free, versatile open-source event-logging
602 software for video/audio coding and live observations. *Methods Ecol. Evol.* **7**, 1325–
603 1330 (2016).

604

605 **Acknowledgments:** We thank M. Alkire, M.M. Chen, J.A. Cheng, and N.T. Nigrin for their
606 assistance with mouse experiments. We also thank additional Hrvatin lab members for
607 their thoughtful input on this project and manuscript. The snRNA-seq and snATAC-seq
608 were performed with the Whitehead Institute Genome Technology Core. Imaging was
609 performed either at the Ragon Institute Microscopy Core, Koch Institute Swanson
610 Biotechnology Center/Microscopy Core, or the Whitehead Institute W.M. Keck Facility for
611 Biological Imaging.

612 **Funding:**

613 Mathers Foundation Grant (S.H.)

614 Searle Scholars Program (S.H.)

615 Pew Charitable Trust (S.H.)

616 Longevity Impetus Grant from Norn Group, Hevolution Foundation and
617 Rosenkranz Foundation (S.H.)

618 MIT Research Support Committee Grant (S.H.)

619 Howard Hughes Medical Institute Hrabowski Scholar (S.H.)

620 **Author Contributions:**

621 Conceptualization: A.J.M, S.H.

622 Methodology: A.J.M, C.M.R, A.J.L.P, W.L., A.S.L., E.C.G, S.H.

623 Investigation: A.J.M, C.M.R, A.J.L.P, W.L., A.S.L.

624 Visualization: A.J.M, C.M.R, W.L., A.S.L.

625 Funding acquisition: S.H., E.C.G

626 Project administration: S.H., E.C.G

627 Supervision: S.H., E.C.G

Writing – original draft: A.J.M, S.H., E.C.G

Writing – review & editing: A.J.M, C.M.R, A.J.L.P, W.L., A.S.L., E.C.G, S.H.

Competing Interests: Authors declare that they have no competing interests.

Data and materials availability: Data will be made available on GEO. All other data needed to evaluate the conclusions are available in the main text, the supplementary materials, available upon request.

Supplementary Materials

Materials and Methods

Figs. S1 to S14

Tables S1 to S3

Movie S1

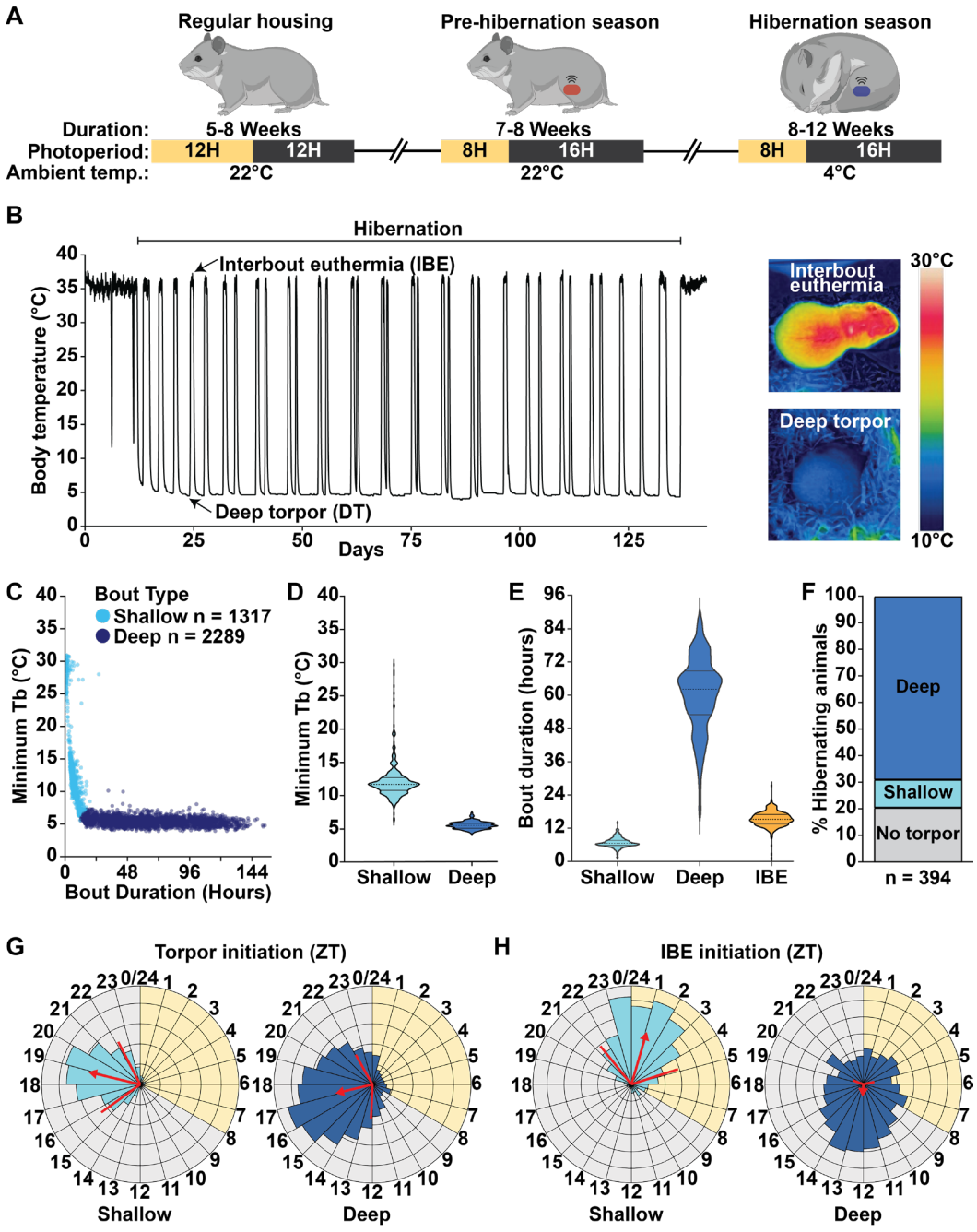

Fig. 1. A laboratory model of Syrian hamster hibernation.

(**A**) A laboratory paradigm for hibernation induction in the Syrian hamster.

(**B**) Left: Representative body temperature trace of a hibernating hamster, consisting of repeated bouts of deep torpor (DT) and interbout euthermia (IBE). Right: Thermal images of a hibernating hamster during euthermic and deep torpor intervals.

(**C**) Classification of torpor bouts as shallow or deep based on minimum temperature and bout duration.

(**D, E**) Violin plots of minimum body temperature (D), and duration (E) of shallow and deep torpor bouts as well as IBE periods (n = 2471).

(**F**) Percentage of animals undergoing DT, only shallow torpor, or no torpor bouts within 6 weeks of initiating the hibernation period.

(**G**) Circadian representation (Raleigh plot) of the time of entry into shallow (light blue) or deep (dark blue) torpor bouts. Light and dark cycle phases are represented by yellow and grey, respectively. Red arrow direction and length indicate mean time of initiation and concentration around the mean, respectively. Red lines flanking the arrow indicate s.d.

(**H**) Circadian representation as in (G) of entry into IBE following deep (left, n = 1496) or shallow (right, n = 1011) torpor bouts.

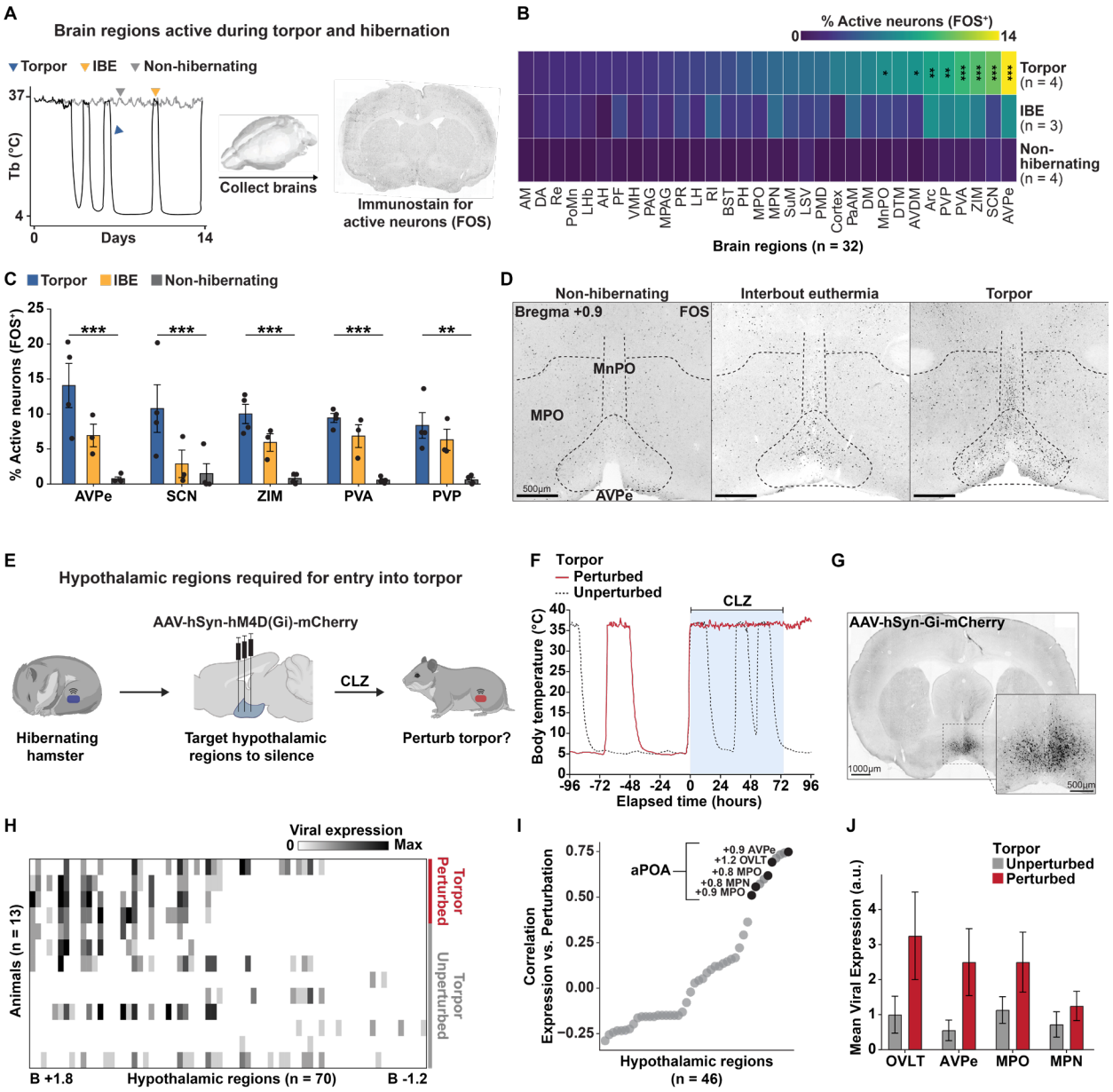

Fig. 2. Identification and functional assessment of deep torpor-active brain regions. (**A**) Strategy for identifying brain regions with hibernation state-dependent activity. Arrows indicate relative sample collection points for torpor, IBE, and non-hibernating animals. (**B, C**) Hypothalamic and thalamic regions demonstrating an increase in FOS-positive cells in torpor as compared to both IBE and non-hibernating controls (*P-adjusted < 0.05, **P-adjusted < 0.01, ***P-adjusted < 0.001).

667 (**D**) FOS immunostaining in the hamster POA across hibernation states. AVPe, MPO, and
668 MnPO denoted by dashed lines.
669 (**E**) Strategy for identifying hypothalamic subregions regulating deep torpor entry.
670 (**F**) T_b traces showing CLZ-mediated disruption of DT in one Gi-DREADD-mCherry-
671 transduced hamster (solid red) but not the other (dashed black).
672 (**G**) Coronal section and inset showing Gi-mCherry expression in the hypothalamus.
673 (**H**) Quantification of regional viral Gi-mCherry expression across injected animals.
674 Hypothalamic regions (n = 70) plotted relative to bregma anterior-posterior coordinates.
675 (**I**) Correlation of regional viral expression across animals with the degree of torpor
676 perturbation identifies the anterior POA (aPOA) as a key DT-regulating region.
677 (**J**) Higher viral Gi-mCherry expression in aPOA regions from animals exhibiting CLZ-
678 dependent torpor disruption (n = 4) compared to unaffected animals (n = 13). Mean ±
679 s.e.m.

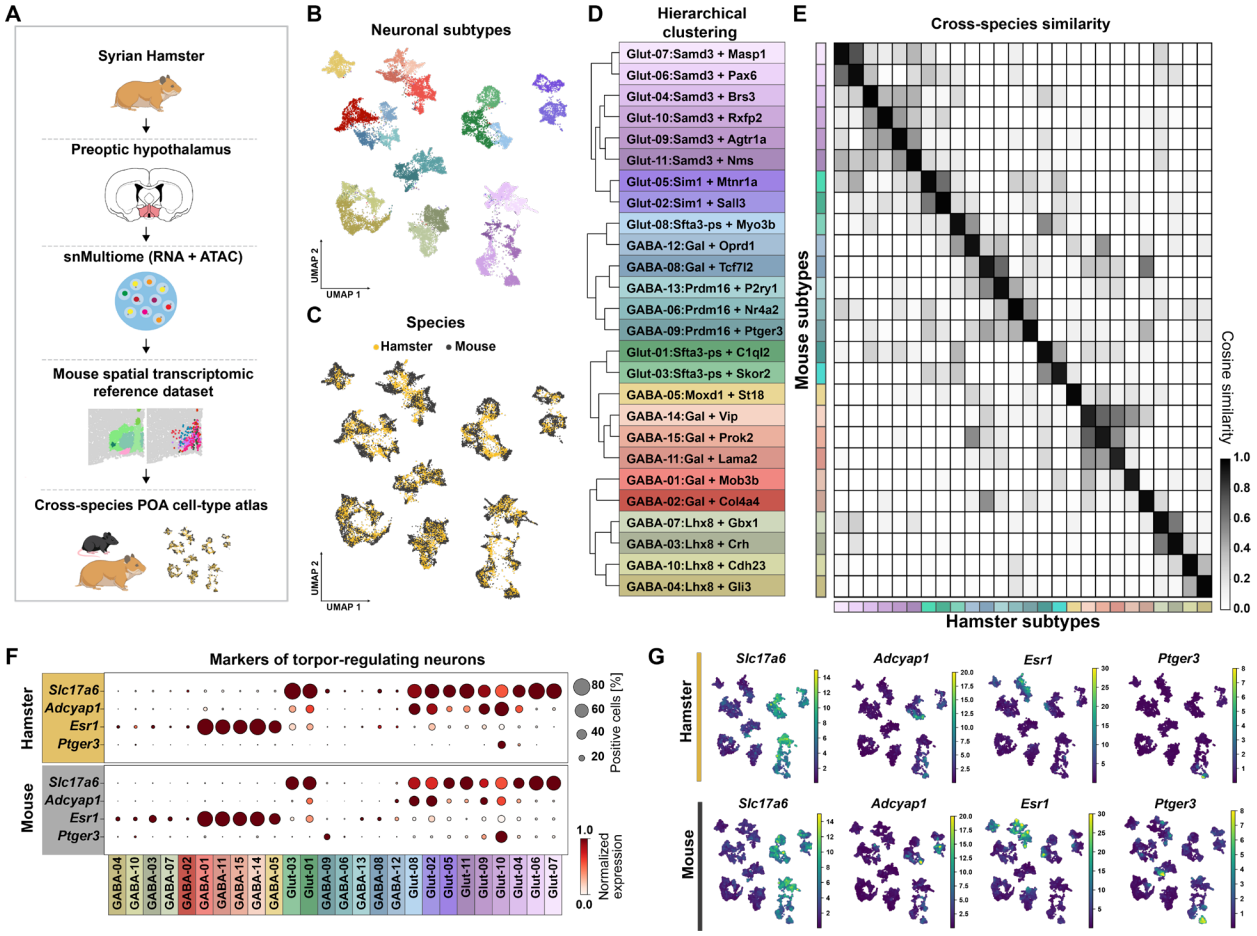
A
Syrian Hamster
Preoptic hypothalamus
snMultiome (RNA + ATAC)
Mouse spatial transcriptomic reference dataset
Cross-species POA cell-type atlas
B
Neuronal subtypes
UMAP 2
UMAP 1
C
Species
Hamster
Mouse
D
Hierarchical clustering
Glut-07:Samd3 + Masp1
Glut-06:Samd3 + Pax6
Glut-04:Samd3 + Brs3
Glut-10:Samd3 + Rxfp2
Glut-09:Samd3 + Agtr1a
Glut-11:Samd3 + Nms
Glut-05:Sim1 + Mtnr1a
Glut-02:Sim1 + Sall3
Glut-08:Sfta3-ps + Myo3b
GABA-12:Gal + Oprd1
GABA-08:Gal + Tcf7l2
GABA-13:Prdm16 + P2ry1
GABA-06:Prdm16 + Nr4a2
GABA-09:Prdm16 + Ptger3
Glut-01:Sfta3-ps + C1ql2
Glut-03:Sfta3-ps + Skor2
GABA-05:Moxd1 + St18
GABA-14:Gal + Vip
GABA-15:Gal + Prok2
GABA-11:Gal + Lama2
GABA-01:Gal + Mob3b
GABA-02:Gal + Col4a4
GABA-07:Lhx8 + Gbx1
GABA-03:Lhx8 + Crh
GABA-10:Lhx8 + Cdh23
GABA-04:Lhx8 + Gli3
E
Cross-species similarity
Mouse subtypes
Hamster subtypes
Cosine similarity
1.0
0.8
0.6
0.4
0.2
0.0
F
Markers of torpor-regulating neurons
Hamster
Mouse
Slc17a6
Adcyap1
Esr1
Ptger3
Positive cells [%]
80
60
40
20
Normalized expression
1.0
0.0
GABA-04
GABA-10
GABA-03
GABA-07
GABA-02
GABA-01
GABA-11
GABA-15
GABA-14
GABA-05
Glut-03
Glut-01
GABA-09
GABA-06
GABA-13
GABA-08
GABA-12
Glut-08
Glut-02
Glut-05
Glut-11
Glut-09
Glut-10
Glut-04
Glut-06
Glut-07
G
Hamster
Mouse
Slc17a6
Adcyap1
Esr1
Ptger3

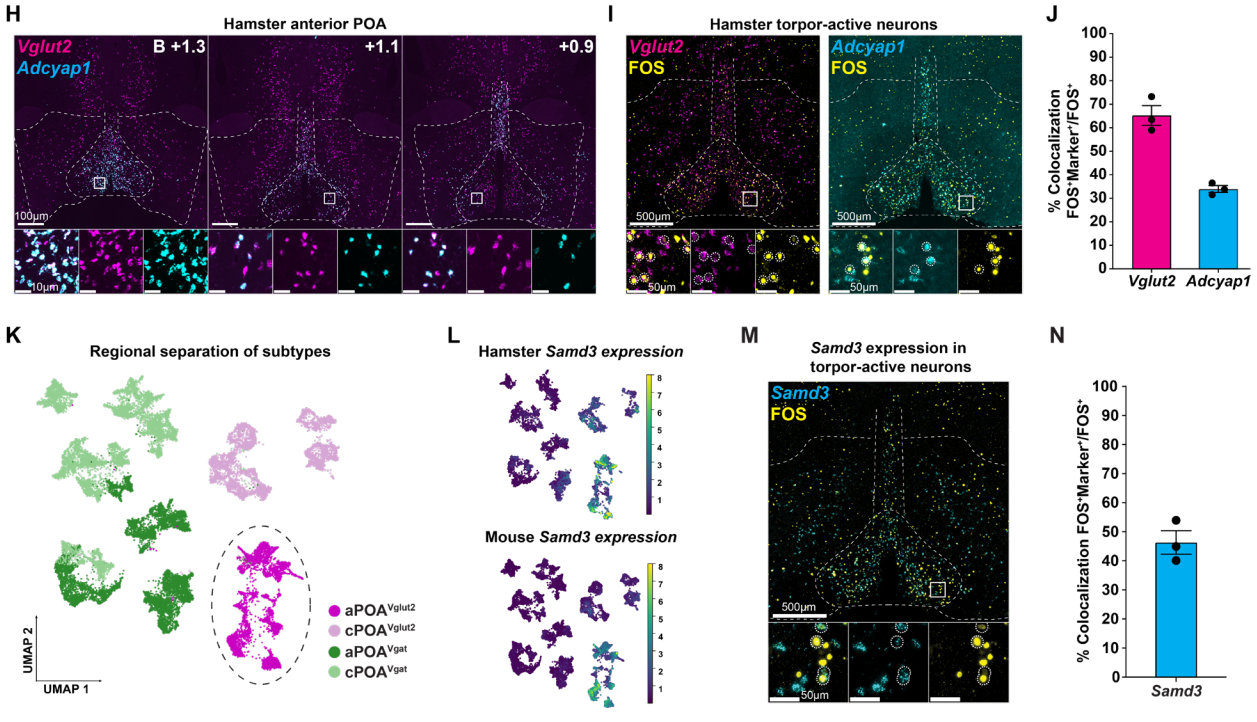
H
Hamster anterior POA
Vglut2
Adcyap1
B +1.3
+1.1
+0.9
100µm
10µm
I
Hamster torpor-active neurons
Vglut2
FOS
Adcyap1
FOS
500µm
50µm
J
% Colocalization FOS+Marker+/FOS+
100
90
80
70
60
50
40
30
20
10
0
Vglut2
Adcyap1
K
Regional separation of subtypes
UMAP 2
UMAP 1
aPOA Vglut2
cPOA Vglut2
aPOA Vgat
cPOA Vgat
L
Hamster Samd3 expression
Mouse Samd3 expression
M
Samd3 expression in torpor-active neurons
Samd3
FOS
500µm
50µm
N
% Colocalization FOS+Marker+/FOS+
100
90
80
70
60
50
40
30
20
10
0
Samd3

681 **Fig. 3. Cell taxonomy and activity mapping implicate glutamatergic aPOA neuronal**
682 **cell types in DT regulation.**
683 (**A**) Workflow to generate a cross-species POA cellular taxonomy.
684 (**B, C**) Uniform manifold approximation and projection (UMAP) plot showing 18,406 nuclei
685 from mice (n = 11) and 8,355 nuclei from Syrian Hamsters (n = 7), indicating 15
686 GABAergic and 11 glutamatergic neuronal subtypes (B) or species of origin (C).
687 (**D**) Hierarchical clustering of the neuronal subtypes.
688 (**E**) Cosine similarity analysis showing pairwise transcriptional relatedness between
689 hamster and mouse neuronal subtypes based on mean gene expression.
690 (**F**) Dot plot showing FIT-associated marker gene expression across mouse and hamster
691 neuronal subtypes.
692 (**G**) UMAP feature plots depicting marker gene expression in the indicated species.
693 (**H**) ISH for select FIT-associated marker genes in hamster aPOA.
694 (**I, J**) Combined FOS immunostaining and ISH analysis for *Slc17a6* (*Vglut2*) and *Adcyap1*
695 from aPOA of hamsters in DT, with accompanying quantification. Mean ± s.e.m.
696 (**K**) UMAP plot annotating hamster and mouse POA neurons by regional location based
697 on mouse MERFISH data.
698 (**L**) UMAP feature plots depicting *Samd3* expression in the indicated species.
699 (**M, N**) Combined FOS immunostaining and *Samd3* ISH analysis of aPOA from hamsters
700 in DT, with accompanying quantification. Mean ± s.e.m.

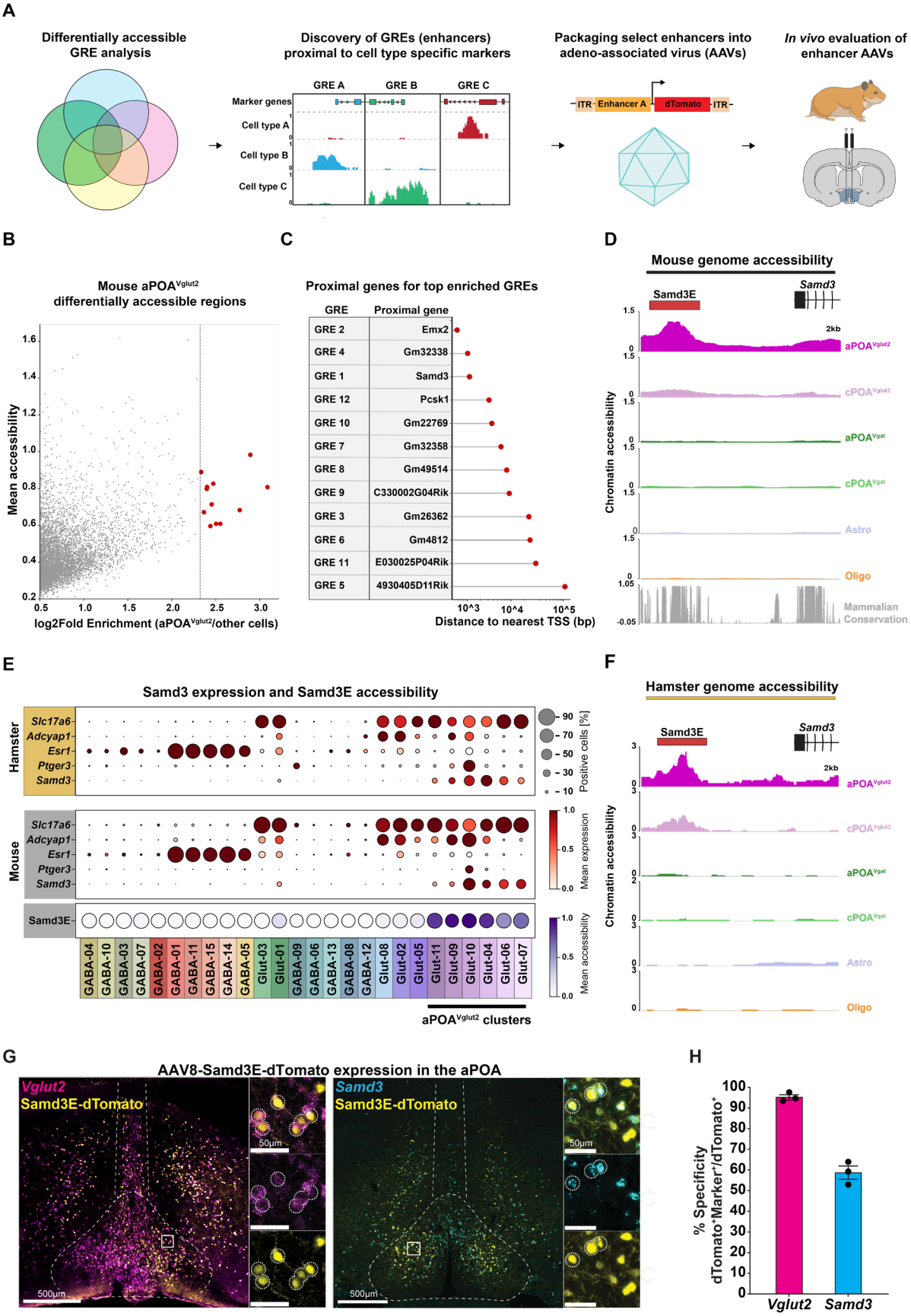
A
Differentially accessible GRE analysis
Discovery of GREs (enhancers) proximal to cell type specific markers
Packaging select enhancers into adeno-associated virus (AAVs)
In vivo evaluation of enhancer AAVs
GRE A
GRE B
GRE C
Marker genes
Cell type A
Cell type B
Cell type C
ITR
Enhancer A
dTomato
ITR
B
Mouse aPOAVglut2 differentially accessible regions
Mean accessibility
log2Fold Enrichment (aPOAVglut2/other cells)
C
Proximal genes for top enriched GREs
GRE
Proximal gene
GRE 2 Emx2
GRE 4 Gm32338
GRE 1 Samd3
GRE 12 Pcsk1
GRE 10 Gm22769
GRE 7 Gm32358
GRE 8 Gm49514
GRE 9 C330002G04Rik
GRE 3 Gm26362
GRE 6 Gm4812
GRE 11 E030025P04Rik
GRE 5 4930405D11Rik
Distance to nearest TSS (bp)
D
Mouse genome accessibility
Samd3E
Samd3
2kb
aPOAVglut2
cPOAVglut2
aPOAVgat
cPOAVgat
Astro
Oligo
Mammalian Conservation
Chromatin accessibility
E
Samd3 expression and Samd3E accessibility
Hamster
Mouse
Slc17a6
Adcyap1
Esr1
Ptger3
Samd3
Samd3E
Positive cells [%]
Mean expression
Mean accessibility
GABA-04
GABA-10
GABA-03
GABA-07
GABA-02
GABA-01
GABA-11
GABA-15
GABA-14
GABA-05
Glut-03
Glut-01
GABA-09
GABA-06
GABA-13
GABA-08
GABA-12
Glut-08
Glut-02
Glut-05
Glut-11
Glut-09
Glut-10
Glut-04
Glut-06
Glut-07
aPOAVglut2 clusters
F
Hamster genome accessibility
Samd3E
Samd3
2kb
aPOAVglut2
cPOAVglut2
aPOAVgat
cPOAVgat
Astro
Oligo
Chromatin accessibility
G
AAV8-Samd3E-dTomato expression in the aPOA
Vglut2
Samd3E-dTomato
Samd3
Samd3E-dTomato
50µm
500µm
H
% Specificity
dTomato+Marker+/dTomato+
Vglut2
Samd3

701

702 **Fig. 4. A novel Enhancer-AAV specifically targeting hamster aPOA^{Vglut2} neurons.**

703 (**A**) Workflow for generation of aPOA^{Vglut2} neuron-selective enhancer-AAVs.

704 (**B**) Scatter plot of genomic elements (n = 15,208) based on differential accessibility in

705 aPOA^{Vglut2} neurons and mean aPOA^{Vglut2} accessibility signal. Top 10 most differentially

706 accessible elements (FDR-corrected $q < 10^{-300}$) highlighted in red.

707 (**C**) Distance to proximal gene transcription start site for the top 10 putative GREs from

708 (B).

709 (**D**) ATAC-seq genome browser tracks (normalized counts per location) for the mouse

710 *Samd3*-proximal putative GRE (*Samd3E,* red box) in the indicated cell populations in

711 mouse, with accompanying sequence conservation below.

712 (**E**) Dotplot depicting *Samd3* gene expression across mouse and hamster POA neuronal

713 subtypes, along with *Samd3E* accessibility in the mouse.

714 (**F**) ATAC-seq genome browser tracks (normalized counts per location) for the hamster

715 *Samd3*-proximal putative GRE (*Samd3E*, red box) in the indicated cell populations in

716 hamster.

717 (**G, H**) Combined immunostaining for viral dTomato and ISH analysis for *Slc17a6* (*Vglut2*)

718 and *Samd3* from aPOA of hamsters injected with AAV8-Samd3E-dTomato, with

719 accompanying quantification. Mean ± s.e.m. (n = 3 animals).

720

721

722

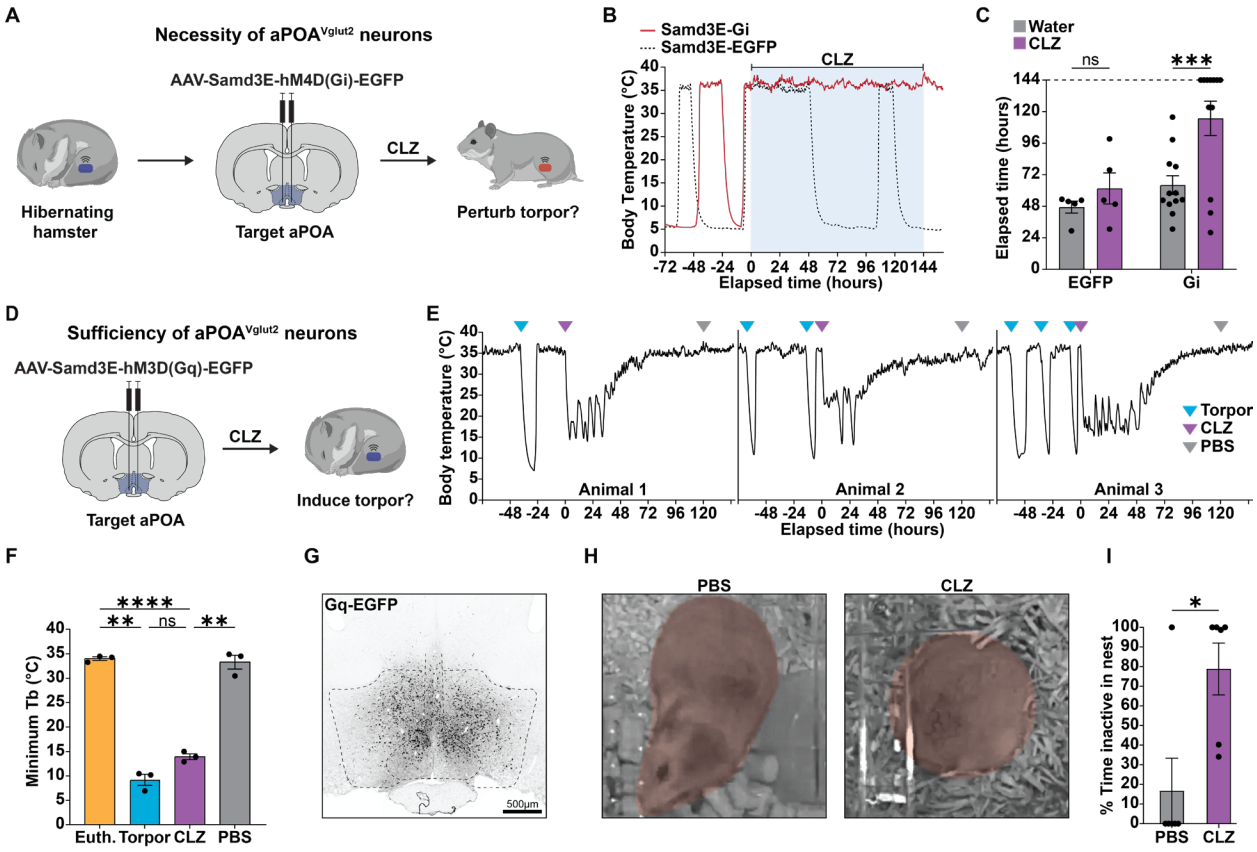

Fig. 5. aPOA^{Vglut2} neuronal activity is necessary and sufficient for hamster deep torpor entry.

(**A**) Strategy for testing the necessity of aPOA^{Vglut2} neuronal activity for DT reentry.

(**B**) T_b traces demonstrating perturbation of torpor resumption upon CLZ administration in Samd3E-Gi-DREADD- but not control Samd3E-EGFP-transduced hamsters.

(**C**) Samd3E-Gi-DREADD-transduced hamsters (n = 12), but not control Samd3E-EGFP-transduced animals (n = 5), show significant perturbations in torpor initiation when administered with CLZ but not water (Šídák's multiple comparisons test).

(**D**) Strategy for testing the sufficiency of aPOA^{Vglut2} neuronal activity for DT entry.

(**E**) T_b traces from Samd3E-Gq-DREADD-injected animals illustrating natural torpor bouts as well as artificial bouts elicited by CLZ administration.

735 (**F**) Quantification of minimum T_b reached in Samd3E-Gq-DREADD-transduced animals
736 during euthermic periods, natural deep torpor, and following administration of CLZ or
737 control PBS (n = 3, Tukey's multiple comparisons test).
738 (**G**) Coronal section showing Samd3E-Gq-DREADD-EGFP expression in the hamster
739 aPOA.
740 (**H**) Images of a Samd3E-Gq-DREADD-transduced hamster following PBS or CLZ
741 treatment.
742 (**I**) Percentage of time Samd3E-Gq-DREADD-transduced animals (n = 6) spent inactive
743 in the nest over a 10 min observation window CLZ or control PBS administration (paired
744 t-test).
745 ****P-adjusted < 0.0001, ***P-adjusted < 0.001, **P-adjusted < 0.01, *P-adjusted < 0.05,
746 ns = not significant).

Supplementary Materials

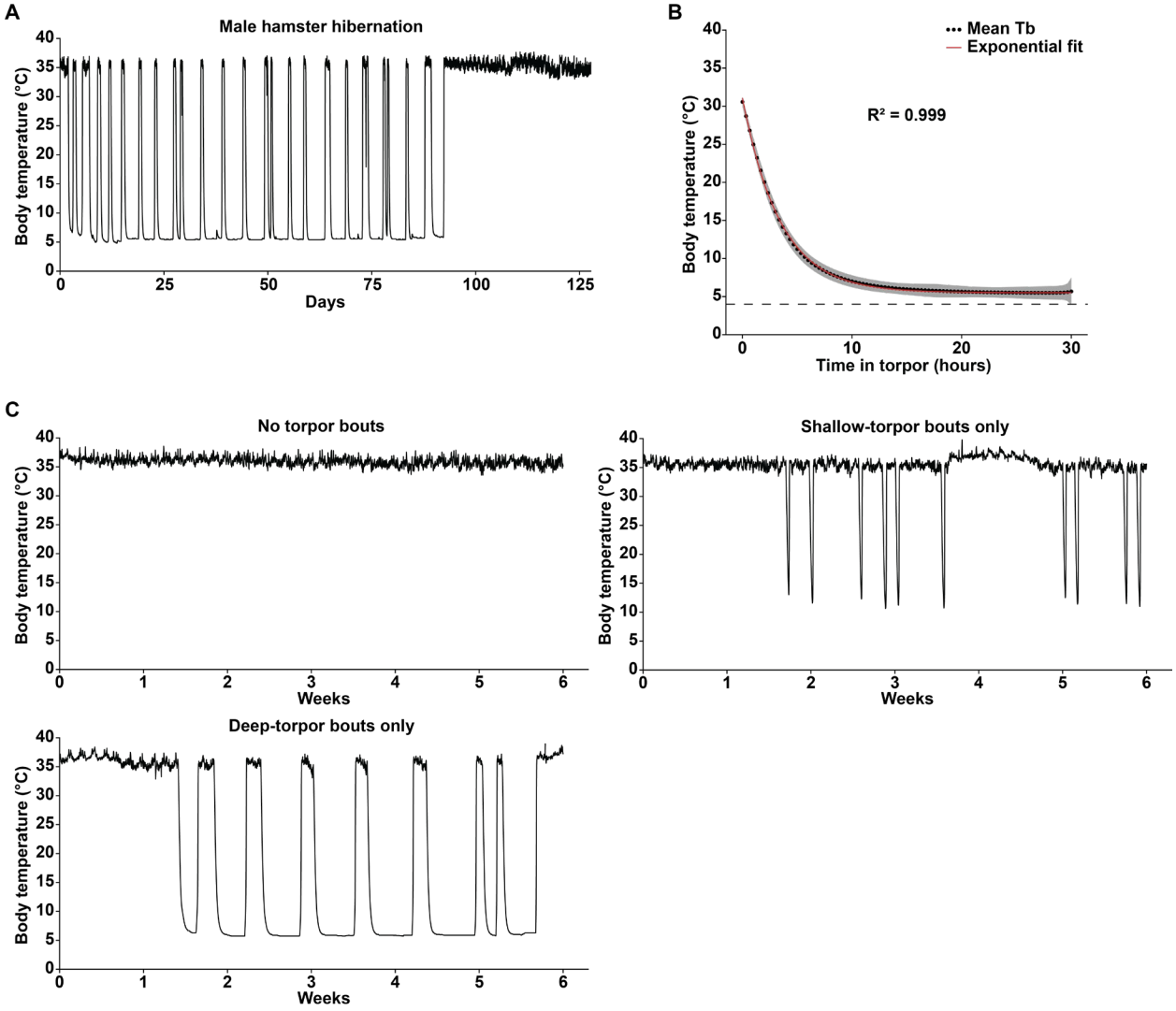

Fig. S1. Core body temperature dynamics during hibernation.

(**A**) Representative core body temperature trace from a male hamster across its hibernation season.

(**B**) Initial T_b decreases during torpor onset follow an exponential decay (animals = 188, torpor bouts = 1262).

(**C**) Body temperature traces from three animals within a 6-week observation period, demonstrating the range of T_b changes.

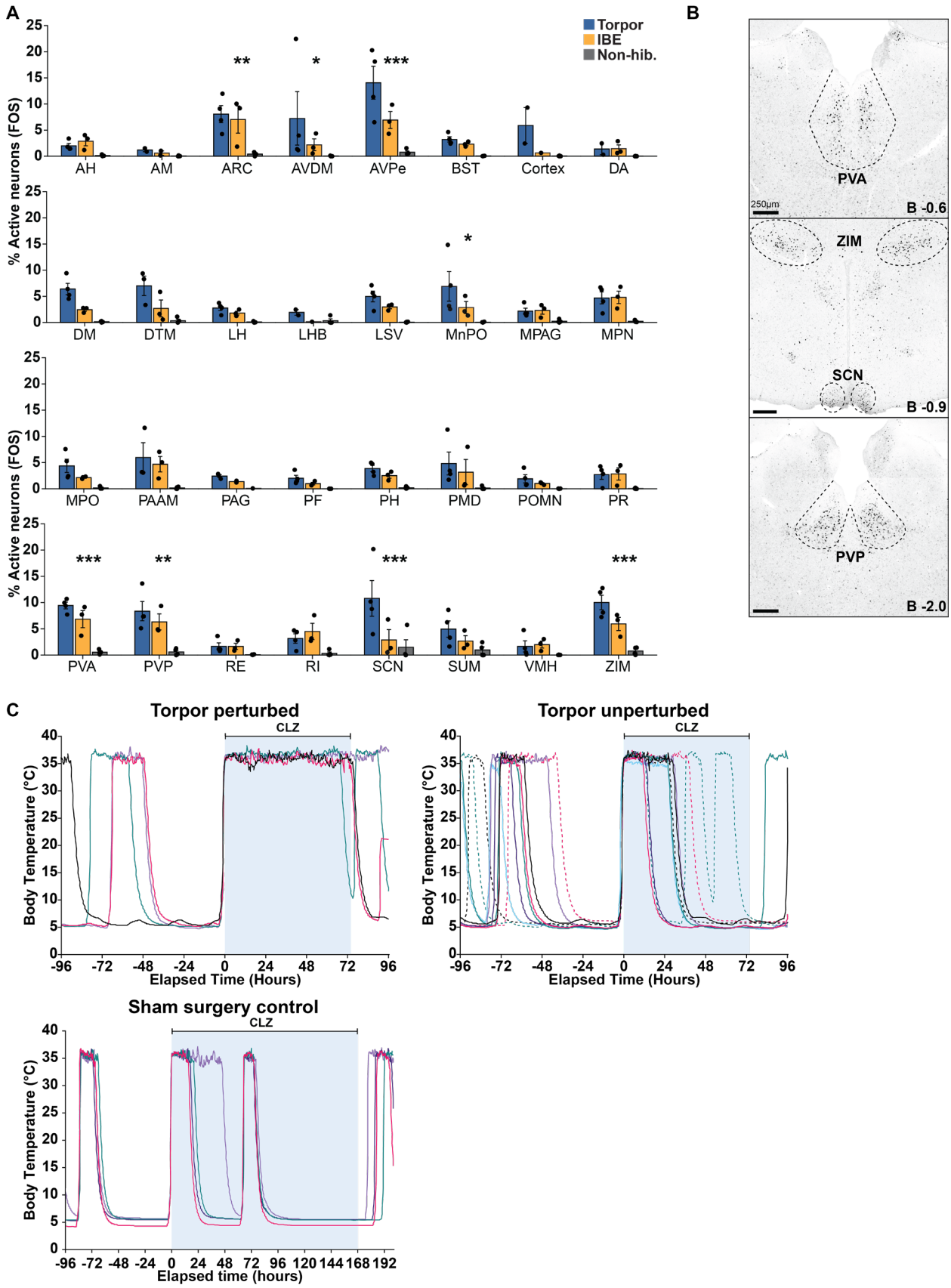
A
Torpor
IBE
Non-hib.
% Active neurons (FOS)
AH
AM
ARC
AVDM
AVPe
BST
Cortex
DA
DM
DTM
LH
LHB
LSV
MnPO
MPAG
MPN
MPO
PAAM
PAG
PF
PH
PMD
POMN
PR
PVA
PVP
RE
RI
SCN
SUM
VMH
ZIM
B
PVA
250µm
B -0.6
ZIM
SCN
B -0.9
PVP
B -2.0
C
Torpor perturbed
Torpor unperturbed
Sham surgery control
CLZ
Body Temperature (°C)
Elapsed Time (Hours)
Elapsed time (hours)

757 **Fig. S2. Hibernation-associated neuronal activity and disruption of torpor entry**
758 **during targeted silencing.**

759 (**A**) Bar plots showing the percent of FOS-expressing neurons across all surveyed regions
760 (n = 32) and hibernation stages (non-hibernating = 3 animals, IBE = 3 animals, torpor =
761 4 animals, p-adjusted < 0.05, **p-adjusted < 0.01, ***p-adjusted < 0.001). Data presented
762 as mean ± s.e.m.

763 (**B**) Representative FOS immunostaining images of an animal in torpor. The top four most
764 deep torpor-active regions after the AVPe are shown: Paraventricular thalamic nucleus
765 anterior (PVA), zona incerta (ZIM), suprachiasmatic nucleus (SCN), and paraventricular
766 thalamic nucleus posterior (PVP).

767 (**C**) Hibernating hamsters (n = 13) were injected with AAV-hSyn-hM4D(Gi)-mCherry,
768 targeting different areas of the anterior hypothalamus. After recovery of DT bouts,
769 clozapine (CLZ, 5 mg/kg) was administered via drinking water. Hamster core body
770 temperature traces are shown, demonstrating CLZ-dependent perturbation of torpor
771 activity in a subset of animals (n = 4) while torpor entry remains unaffected in other
772 animals (n = 9).

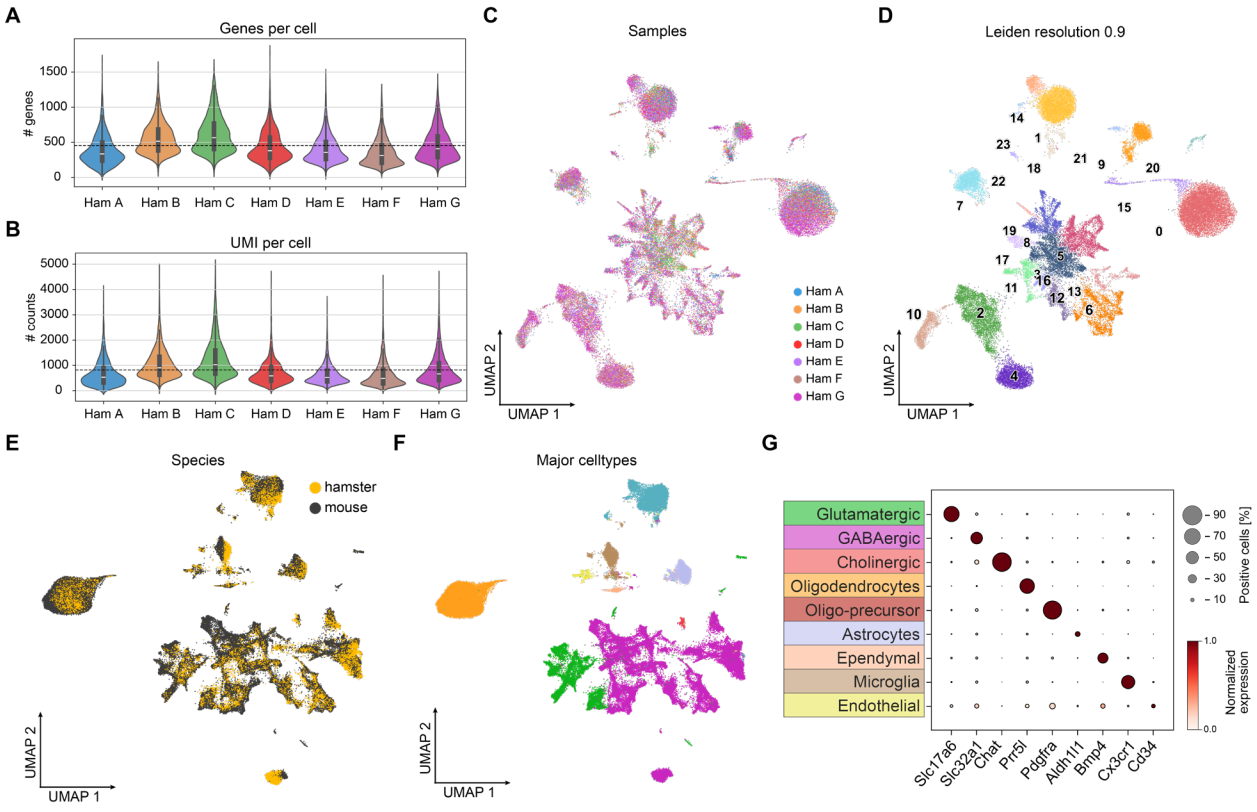

Fig. S3. snRNA-seq analysis of hamster and mouse POA and separation of major neuronal and non-neuronal cell types.

Our snRNA-seq and snATAC-seq data from hamster POA samples were first aligned with the mouse POA multiome dataset from Kaplan et. al (*60*), separating major neuronal and non-neuronal cell types from both datasets.

(**A, B**) Violin plots showing the number of detected genes (A) and unique transcripts (UMIs) (B) per cell in each hamster snRNA-seq sample.

(**C, D**) UMAP plots showing 43,243 nuclei across 7 hamster samples and their Leiden clustering.

(**E, F**) UMAP plots showing an integrated dataset containing 45,553 hamster and mouse nuclei, and their separation into major cell types.

785 (**G**) Dot plot showing the expression of select gene markers of each major neuronal and
786 non-neuronal cell type. Color indicates gene expression scaled across different cell types.
787 Circle size indicates the percentage of cells expressing each marker gene.
788

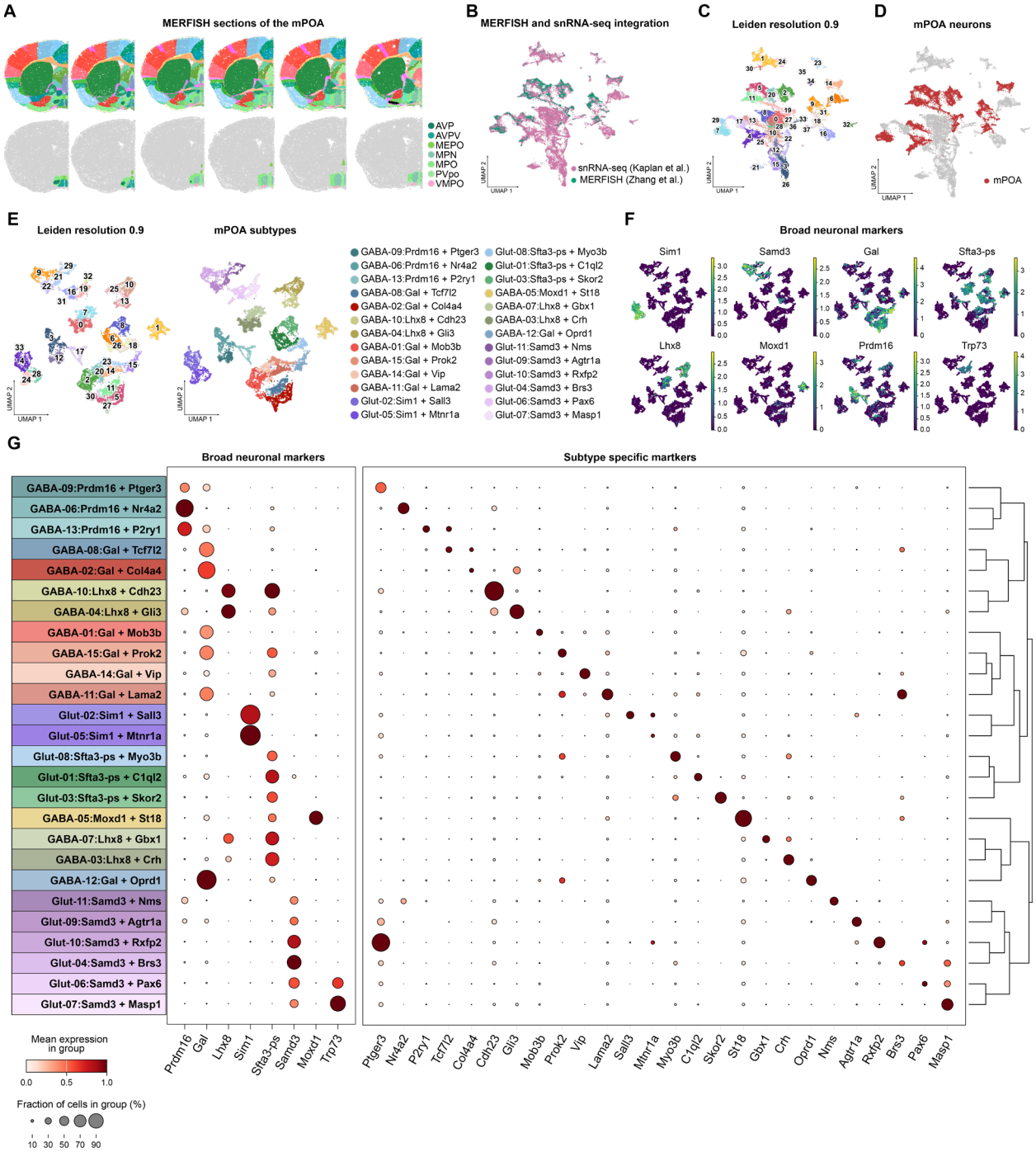

Fig. S4. Creation of a mouse mPOA reference transcriptomic dataset.

A mouse reference transcriptomic dataset restricted to cell types in our target regions – the medial and median POA (mPOA) – was generated. To this end, mouse spatial transcriptomic data (MERFISH) (*61*) was subset to only include neurons found in the

794 mPOA and co-clustered with mouse neuronal snRNA-seq populations from **Fig. S3F, G**,
795 enabling the annotation of 15 GABAergic and 11 glutamatergic mPOA neuronal
796 populations in the mouse snRNA-seq dataset.
797 (**A**) Coronal brain sections indicating subregions of the mPOA. MERFISH data was
798 subset to only include neurons within the indicated mPOA regions.
799 (**B**) UMAP plot showing the integrated MERFISH mPOA and mouse snRNA-seq dataset.
800 (**C, D**) UMAP plot showing Leiden clustering (C) and regional annotation (D) of the
801 integrated MERFISH mPOA and mouse snRNA-seq dataset.
802 (**E**) UMAP plot of only mPOA neurons from (D) colored by Leiden cluster number (left),
803 or annotated clusters (right). Annotation comprises cell class (Glut = glutamatergic, GABA
804 = GABAergic), followed by key marker genes. These cells comprise the mouse mPOA
805 reference transcriptomic dataset.
806 (**F**) UMAP plot showing expression of select marker genes in mouse mPOA.
807 (**G**) Dot plot showing the expression of cell-type-specific marker genes in mouse mPOA.

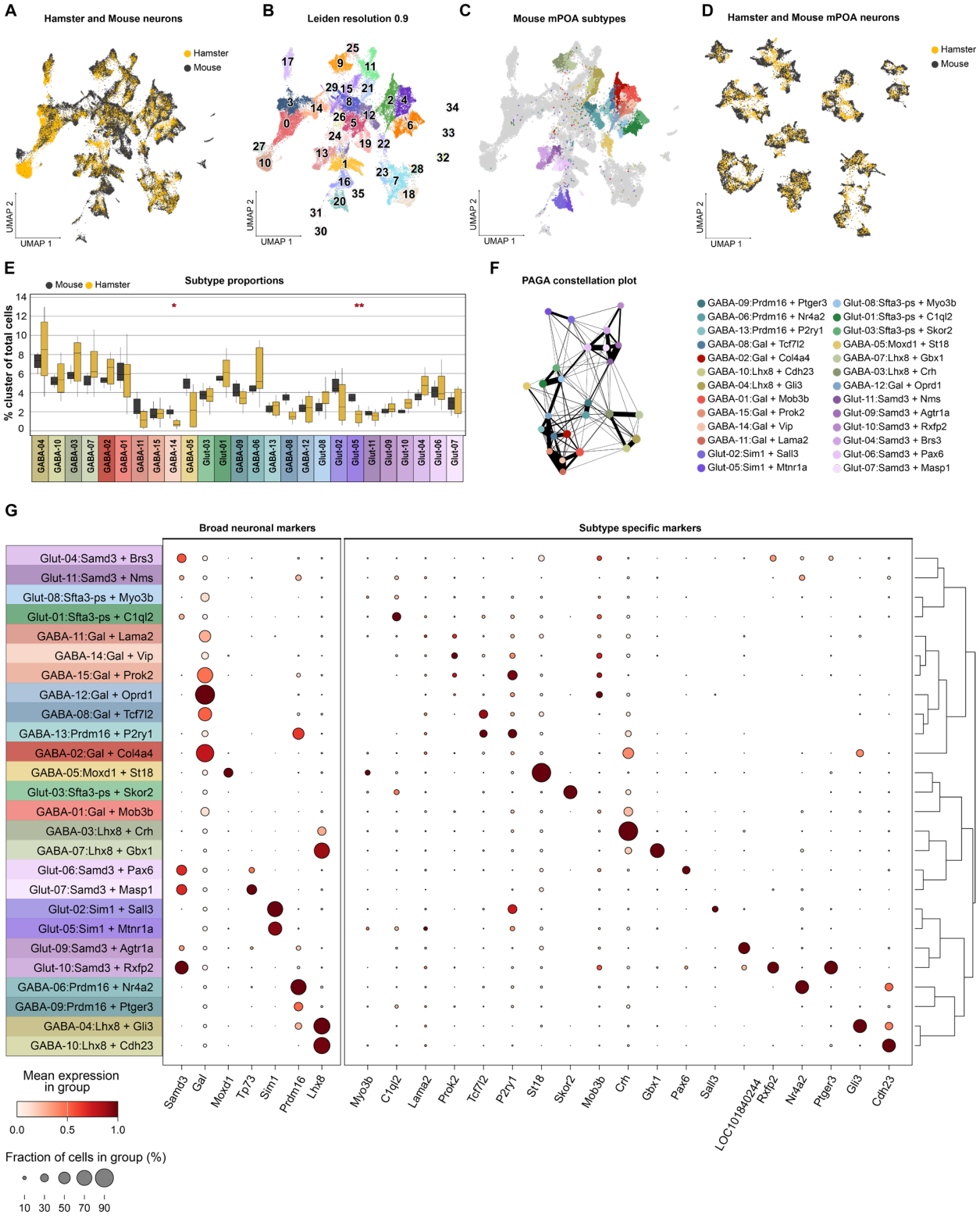

Fig. S5 Integration of hamster snRNA-seq with the mouse mPOA reference transcriptomic dataset.

811 Leveraging the annotations from the mouse mPOA reference transcriptomic dataset (**Fig**
812 **S4**), we annotated neurons from the hamster POA snRNA-seq dataset to generate the
813 final cross-species atlas.
814 (**A, B**) UMAP plot showing integrated hamster and mouse neuronal snRNA-seq data,
815 colored by species of origin (A), or Leiden cluster (B).
816 (**C**) UMAP plot highlighting the location of mouse mPOA neurons, colored based on
817 clusters from the mouse mPOA reference transcriptomic dataset.
818 (**D**) UMAP plot as in **Fig. 3** displaying all mouse and hamster mPOA neurons from the
819 snRNA-seq dataset, colored by the clusters defined in the mouse mPOA reference
820 transcriptomic dataset.
821 (**E**) Relative abundance of each cell type in the mouse and hamster POA dataset. Three
822 cell types show significant differences in abundance (* $P < 0.05$, ** $P < 0.01$, Mann-
823 Whitney U test).
824 (**F**) Constellation plot showing the relationships between subtypes based on their latent
825 space.
826 (**G**) Dot plot showing the expression of cell-type-specific marker genes for hamster
827 neurons.

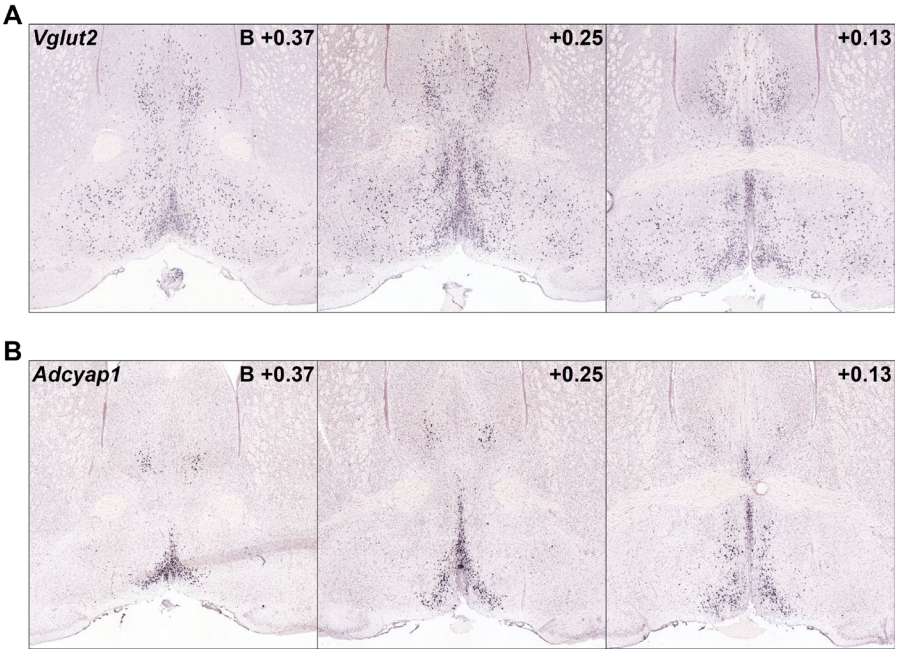

Fig. S6. Anatomical distribution of mouse FIT-associated neurons.

(**A, B**) Example coronal sections of the mouse brain containing the anterior POA, showing ISH signal for marker genes *Slc17a6/Vglut2* (A) and *Adycap1* (B). Data from mouse.brain-map.org (*75*).

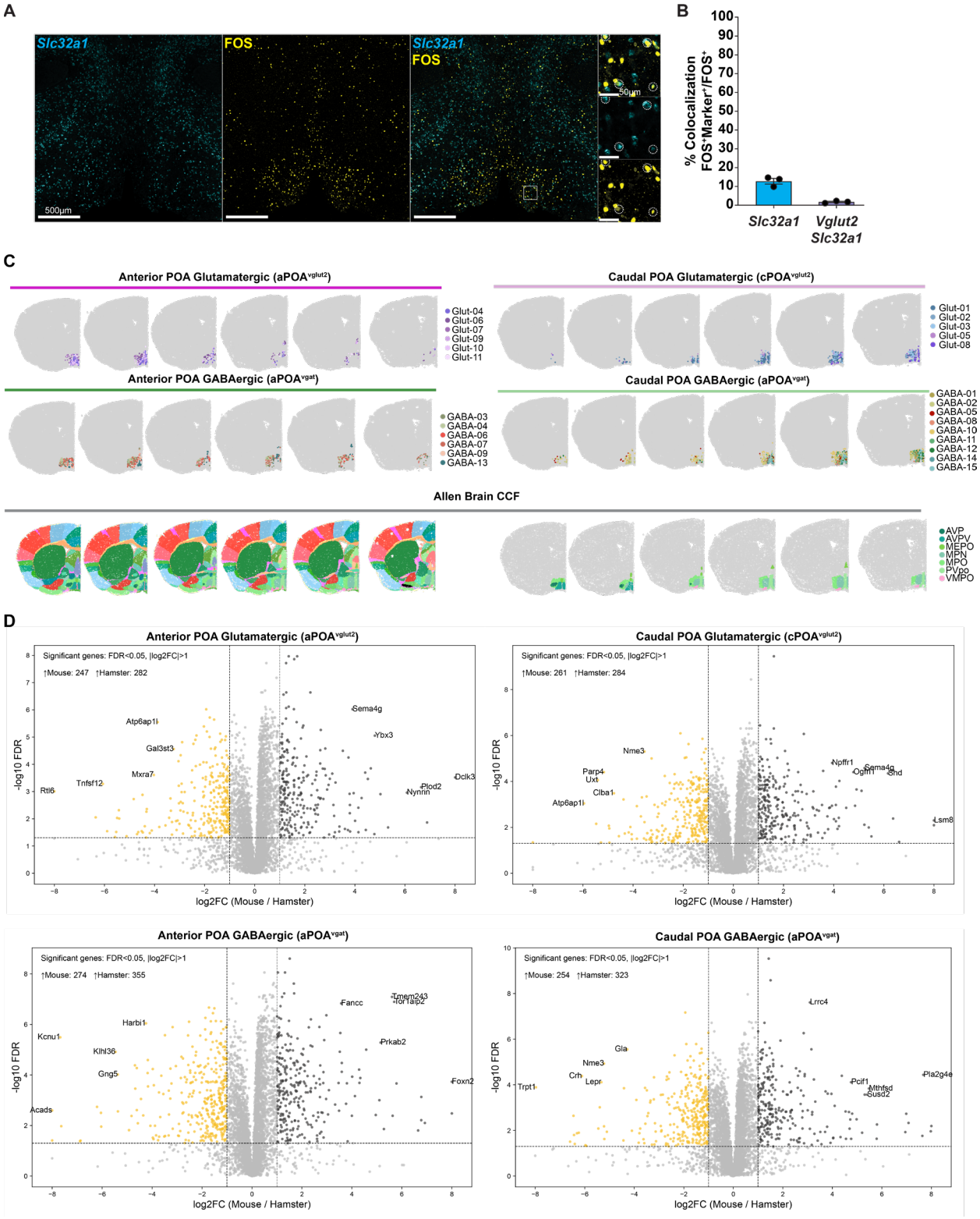

Fig. S7. Marker expression of DT-active neurons; anatomical localization and cross-species differential gene expression of POA neuronal populations.

836 (**A**) Example coronal sections showing the aPOA of a Syrian hamster collected during DT
837 onset. Immunofluorescent staining against FOS indicates the location of active neurons
838 (yellow), whereas ISH indicates the expression of the marker gene *Slc32a1* (*Vgat*). High-
839 magnification images are shown as insets with example FOS+ *Slc32a1*+ cells circled.
840 (**B**) Quantification of the fraction of FOS+ neurons during torpor that express *Slc32a1*
841 (12.8% ± 1.5, animals = 3) and dual-expressing *Slc17a6/Slc32a1* (1.8% ± 0.3, n = 3)
842 neurons. Data presented as mean ± s.e.m.
843 (**C**) MERFISH plot showing the spatial distribution of neuronal subtypes in the mouse
844 POA separated by their major cell types and anatomical location.
845 (**D**) Differential gene expression between hamster and mouse neurons across the four
846 major neuron groups.

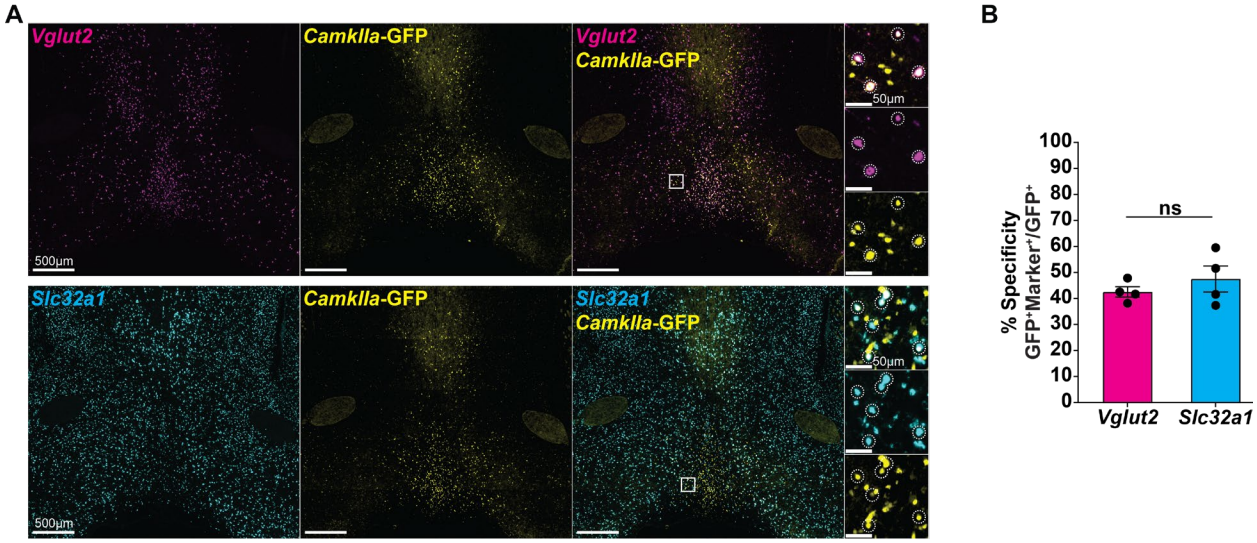

Fig. S8. *CamkIIa* promoter-based AAVs lack specificity for glutamatergic neurons in the hamster aPOA.

Hamsters (n = 4) were stereotaxically administered AAV8-CamkIIa-GFP and harvested ~2 weeks later for immunostaining and ISH.

(**A**) Example coronal sections showing the hamster POA comprising AVPe, MPA, and MnPO. Immunofluorescent staining against GFP indicates the location of virally labeled cells (yellow), whereas ISH indicates the expression of genes *Slc17a6* (*Vglut2; magenta*) and *Slc32a1 (Vgat; cyan)*. High-magnification images are shown on the right with example GFP+ *Marker*+ cells circled.

(**B**) Quantification of the fraction of AAV-CamkIIa-GFP+ neurons that express *Slc17a6* (42.6% ± 2.0, animals = 4), and *Slc32a1* (47.5 ± 5.0%, animals = 4). Data presented as mean ± s.e.m.

A

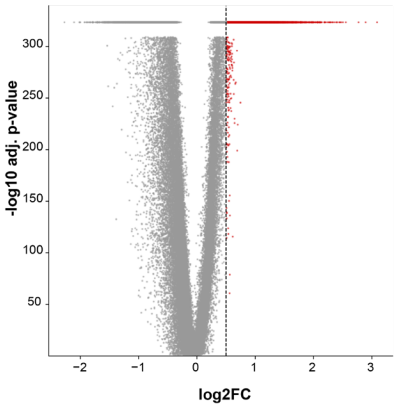

B

	Genomic coordinates (mm10)	Nearest gene
GRE 1	chr10:26228096-26228596	Samd3
GRE 2	chr19:59457295-59457795	Emx2
GRE 3	chr6:111965822-111966322	Gm26362
GRE 4	chr10:41139206-41139706	Gm32338
GRE 5	chr11:91056877-91057377	4930405D11Rik
GRE 6	chr13:69317802-69318302	Gm4812
GRE 7	chr16:96450604-96451104	Gm32358
GRE 8	chr16:23505809-23506309	Gm49514
GRE 9	chr19:23085045-23085545	C330002G04Rik
GRE 10	chr16:63743408-63743908	Gm22769
GRE 11	chr11:109106715-109107215	E030025P04Rik
GRE 12	chr13:75113945-75114445	Pcsk1

C

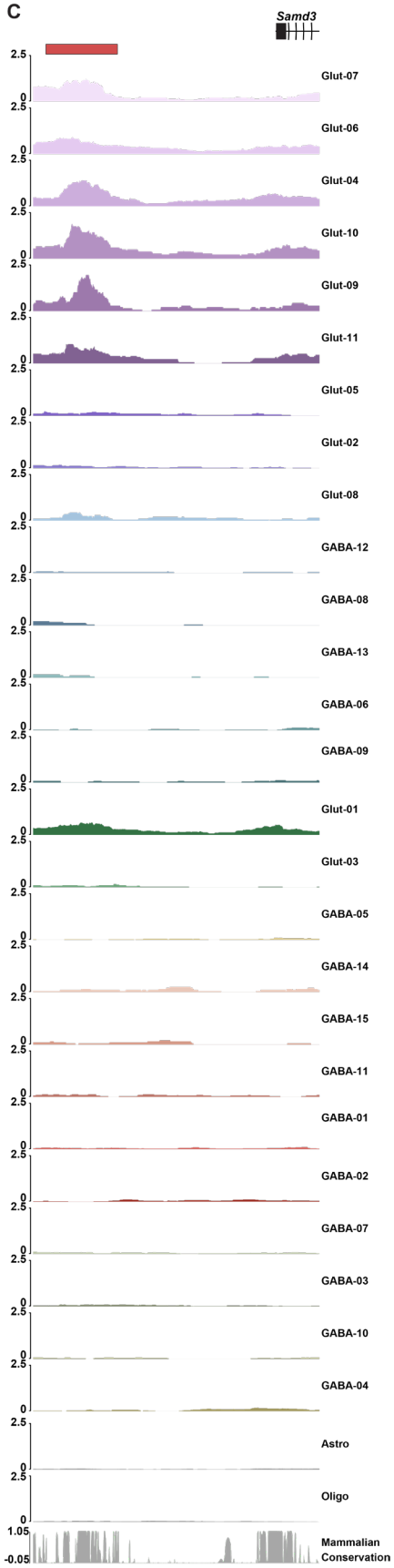

D

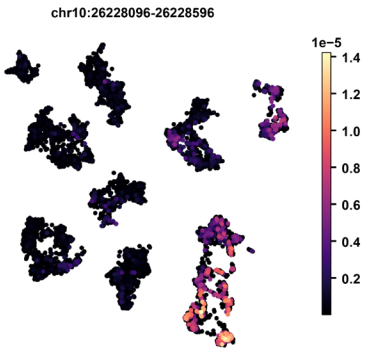

E

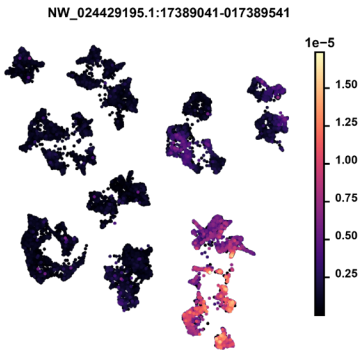

861 **Fig. S9 snATAC-seq analysis reveals *Samd3E* as tool to target POA neurons.**

862 (**A**) Differential accessibility analyses of genomic elements in aPOA^{Vglut2} neurons vs. all

863 other neurons in mice; top regions (log2FC > 0.5) are marked in red for further analysis.

864 (**B**) Genomic location and nearest gene of the top candidate putative GREs.

865 (**C**) ATAC-seq genome browser tracks (normalized counts per location) of individual

866 mouse neuronal subtypes showing the mouse *Samd3*-proximal putative GRE (*Samd3E,*

867 red box), with accompanying sequence conservation below.

868 (**D, E**) UMAP feature plots depicting *Samd3E* accessibility in the indicated species.

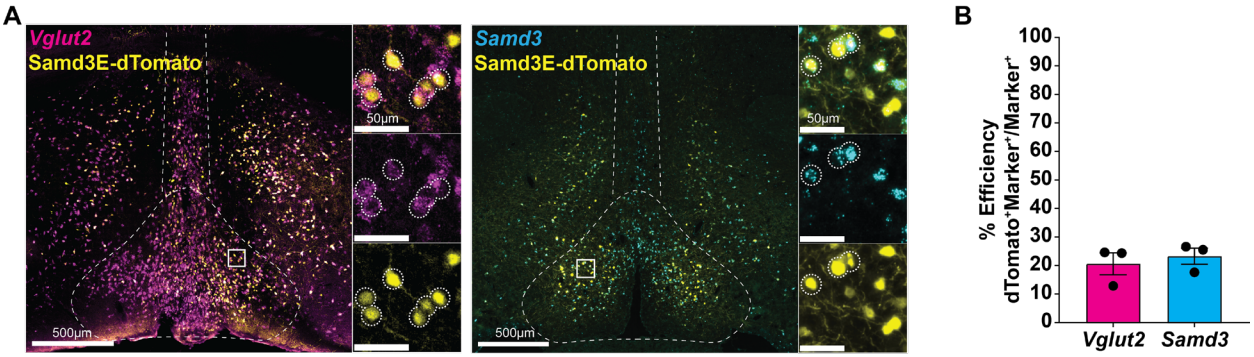

Fig. S10 Samd3E-AAV transduction efficiency.

(**A**) Efficiency of targeting aPOA^{Vglut2} and aPOA^{Samd3} neurons with AAV8-Samd3E-dTomato. Syrian hamsters (n = 3) were injected with AAV8-Samd3E-dTomato. Immunofluorescent staining against dTomato was used to identify virally labeled cells (yellow), whereas ISH indicates the expression of the marker gene *Slc17a6* (*Vglut2*, magenta) and *Samd3* (cyan), as in **Fig. 4G**.

(**B**) Quantification of the fraction of *Slc17a6*+ cells that also express dTomato+ (20.6 ± 3.9%, animals = 3) and *Samd3*+ cells that also express dTomato+ (23.3 ± 2.8%, animals = 3). Given limited viral spread, this quantification was limited to the area of viral expression within the aPOA. These results indicate that AAV8-Samd3E-dTomato achieves high specificity and modest efficiency for targeting aPOA^{Vglut2} and aPOA^{Samd3} neurons.

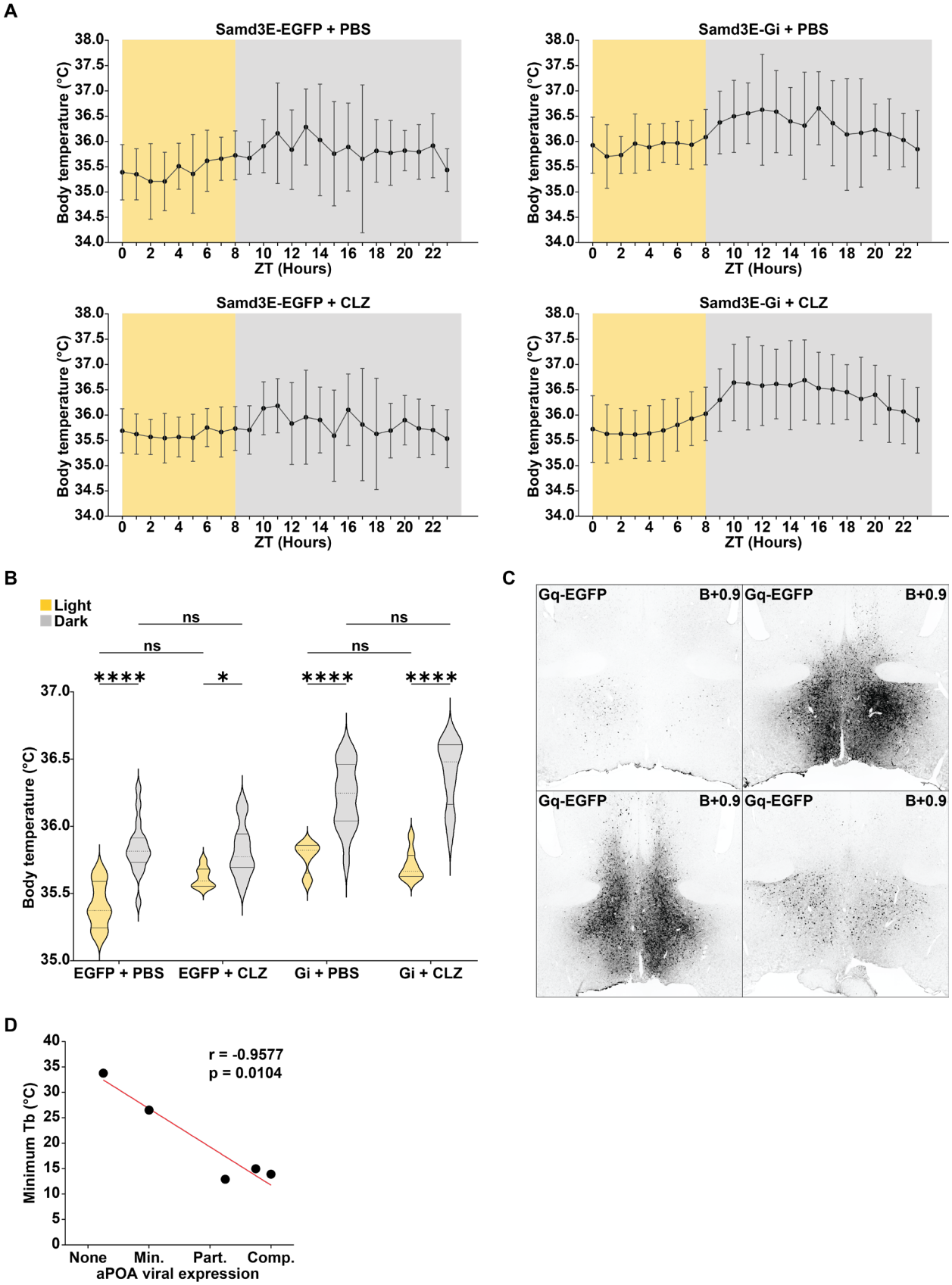
A
Samd3E-EGFP + PBS
Samd3E-Gi + PBS
Samd3E-EGFP + CLZ
Samd3E-Gi + CLZ
Body temperature (°C)
ZT (Hours)
B
Light
Dark
ns
****
*
EGFP + PBS
EGFP + CLZ
Gi + PBS
Gi + CLZ
C
Gq-EGFP
B+0.9
D
r = -0.9577
p = 0.0104
Minimum Tb (°C)
None
Min.
Part.
Comp.
aPOA viral expression

882

883 **Fig. S11. Circadian T_b patterns and correlation between viral aPOA expression and**
884 **T_b decrease.**
885 (**A**) Circadian fluctuation of T_b in Samd3E-EGFP- and Samd3E-Gi-DREADD-injected
886 hamsters following administration of CLZ (5 mg/kg) or control PBS. Light and dark cycle
887 phases are represented by yellow and grey, respectively. Data presented as mean ± s.d.
888 of core body temperatures during each hour.
889 (**B**) Violin plot quantification of body temperature range between light (yellow) and dark
890 (grey) phases of Samd3E-EGFP- (n = 5 animals) or Samd3E-Gi-DREADD-injected
891 animals (n = 12) following CLZ or control PBS administration (Tukey's multiple
892 comparisons test; *P-adjusted < 0.05, ****P-adjusted < 0.0001, ns = not significant P >
893 0.05).
894 (**C**) Immunofluorescence images in the aPOA of additional Samd3E-Gq-DREADD-EGFP-
895 injected animals.
896 (**D**) Correlation between minimum T_b reached following CLZ administration and viral
897 expression within the aPOA (n = 5 animals, r = -0.95, P = 0.01).

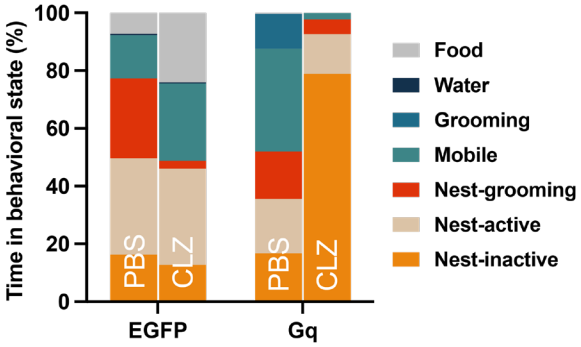

Fig. S12. Changes in behavioral repertoire after aPOA^{Vglut2} neuronal activation. Percentage of time in behavioral states over a 10 min observation window post-injection with PBS or CLZ across all hamsters injected with AAV-Samd3E-EGFP-P2A-Synaptophysin-mRuby (n = 3) and AAV-Samd3E-hM3D(Gq)-nlsGFP (n=6).

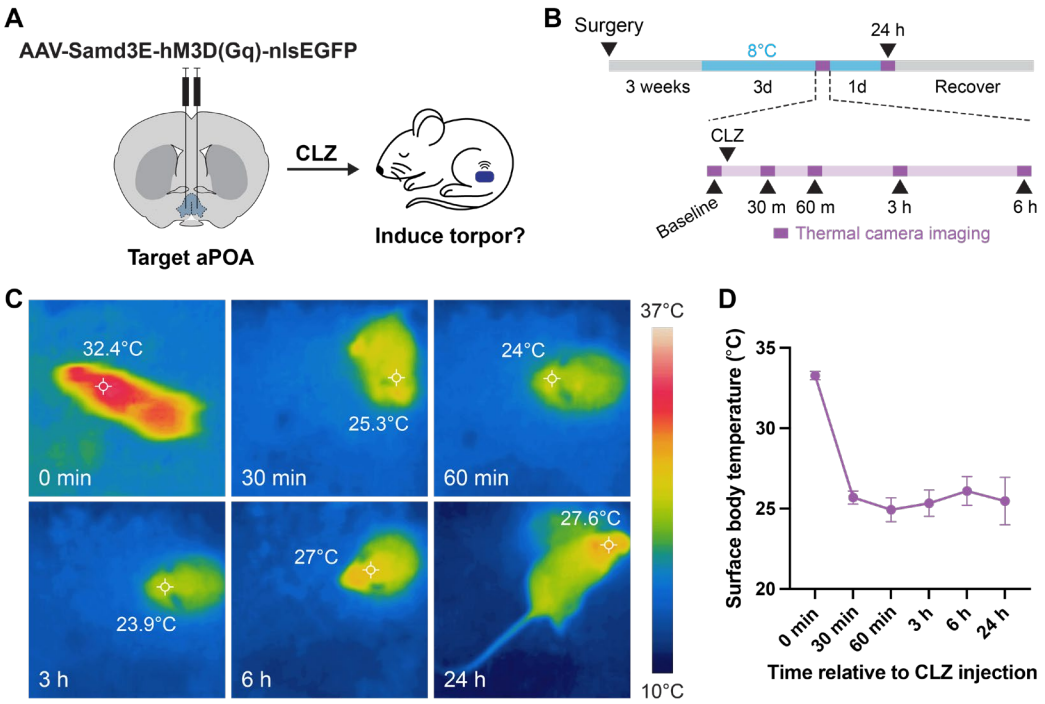

Fig S13. Stimulation of aPOA^{Vglut2} neurons in mice and resulting body temperature change.

(**A**) Schematic of experimental design.

(**B**) Timeline of experiment and analysis. Mice were acclimated to 8°C for 3 days before injection with CLZ (5 mg/kg) and imaged with a thermal camera at baseline, 30 min, 60 min, 3 hours, 6 hours, and 24 hours post injection at 8°C.

(**C**) Representative thermographic images obtained by chemogenetic stimulation of aPOA^{Vglut2} neurons.

(**D**) Surface body temperature before (0 min) and after (30 min to 24 h) CLZ injection (n=7 mice). Data are presented as mean ± s.e.m.

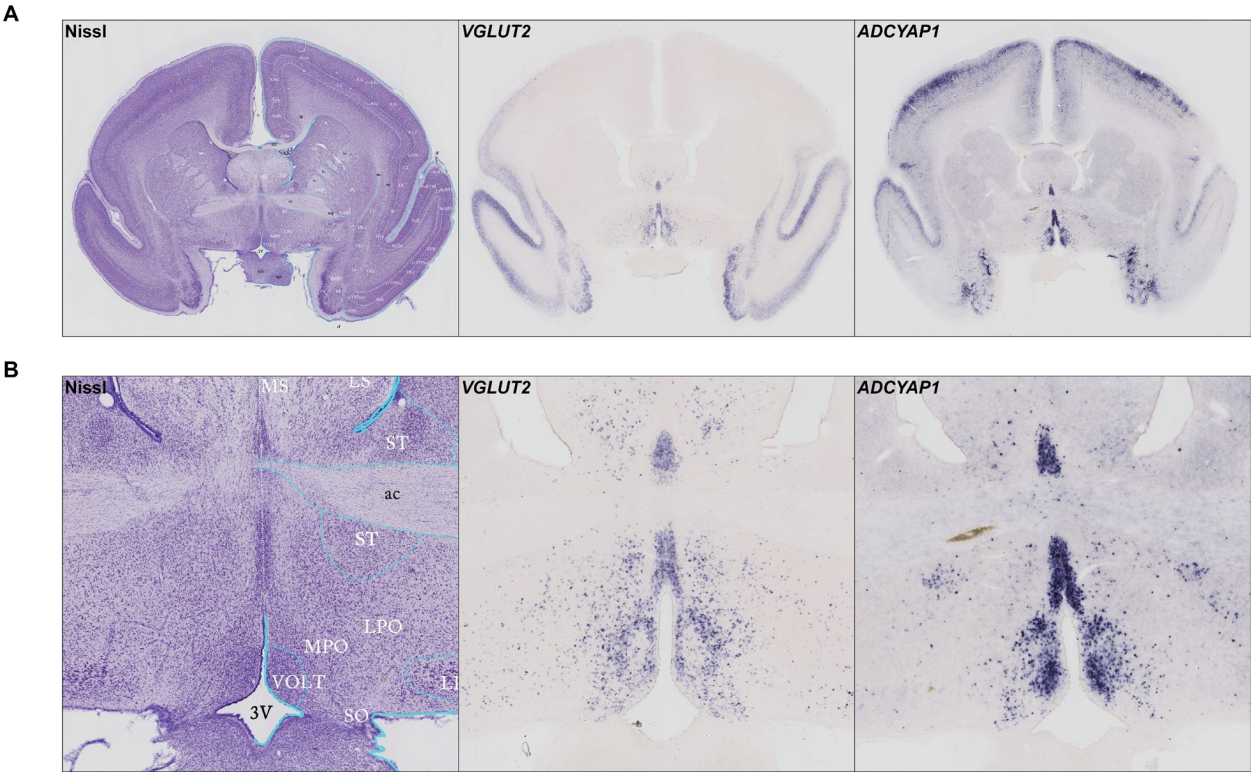

Fig S14. *In situ* hybridization for marker of torpor-associated genes in marmosets. (**A**) Example coronal sections of the marmoset brain containing the anterior POA showing ISH signal for marker genes *Slc17a6/Vglut2* and *Adycap1*.

(**B**) Higher resolution images from (A) displaying the anterior POA. Data from https://gene-atlas.brainminds.jp/ (*72–74*).

Region abbreviation	Region full name
AH	anterior hypothalamic area
AM	anteromedial thalamic nucleus
ARC	arcuate hypothalamic nucleus
AVDM	anteroventral thalamic nucleus dorsomedial
AVPe	anteroventral periventricular nucleus
BST	bed nucleus of the stria terminalis
CORTEX	cerebral cortex
DA	dorsal hypothalamic area
DM	dorsomedial hypothalamic nucleus
DTM	dorsal tuberomammillary nucleus
LH	lateral hypothalamic area
LHB	lateral habenular nucleus
LSV	lateral septal nucleus ventral
MnPO	median preoptic nucleus
MPN	medial preoptic nucleus
MPO	medial preoptic area
PAAM	paraventricular hypothalamic nucleus anterior magnocellular
PAG	periaqueductal gray
PF	parafascicular thalamic nucleus
PH	posterior hypothalamic nucleus
PMD	premammillary nucleus dorsal
POMN	posteromedian thalamic nucleus
PR	prerubral field
PVA	paraventricular thalamic nucleus anterior
PVP	paraventricular thalamic nucleus posterior
RE	reuniens thalamic nucleus
RI	rostral interstitial nucleus of the medial longitudinal fasciculus
SCN	suprachiasmatic nucleus
SUM	supramammillary nucleus
VMH	ventromedial hypothalamic nucleus
ZIM	zona incerta medial

920 **Table S1. Brain region abbreviations**

921 **Methods**

922 **Animals**

923 Animal experiments were approved by the Massachusetts Institute of Technology
924 Committee of Animal Care (Protocol 2503000788), following ethical guidelines described
925 in the US National Institutes of Health Guide for the Care and Use of Laboratory Animals
926 and the Animal Welfare Act.

927 **Hamster.** For all experiments, unless otherwise noted, adult female (5-6-week-
928 old) Syrian hamsters (Inotiv, Strain HsdHan:AURA, Stock 089) were used. Hamsters
929 were singly caged and initially housed at 22°C under a standard 12-hour light/dark cycle
930 (12L:12D) cycle in temperature- and humidity-controlled rooms and had *ad libitum* access
931 to food and water.

932 **Mouse.** Adult female (8-week-old) C57BL/6J (JAX #000664) mice were used. All
933 mice were group housed initially at 22°C under a standard 12L:12D cycle in temperature-
934 and humidity-controlled rooms and had *ad libitum* access to food and water.

935 No statistical methods were used to predetermine the sample size. Hamsters were
936 randomly assigned to experimental groups before surgery. Where possible, investigators
937 were blinded during analysis.

938

939 **Hibernation Induction**

940 Utilizing a modified hibernation paradigm (*15*, *76*) female (5-6-week-old) hamsters
941 were singly caged and housed at 22°C under a standard 12L:12D cycle for a short period
942 to acclimate to the animal facility. Upon completion of acclimation, hamsters were
943 transferred to a reduced 8L:16D cycle with an ambient temperature of 22°C. After 7-8

944 weeks, hamsters were placed in temperature-controlled chambers with 8L:16D cycle and
945 ambient temperatures of 4-5°C. Initiation of hibernation was confirmed by changes in T_b
946 measured by telemetric temperature probes. In all cases, hamsters had *ad libitum* access
947 to food and water.
948
949 **Telemetric monitoring of core body temperature**
950 Within the 7-8-week period of housing at 22°C in 8L:16D cycle, hamsters were
951 anesthetized with 3% isoflurane and implanted with telemetric/logger temperature probes
952 (Star-Oddi, DST microRF-T) in the abdominal cavity. Hamsters were allowed to recover
953 for a minimum of three days before additional procedures or experiments were performed.
954 After recovery and at the end of the 7-8-week period, hamsters were moved to
955 temperature-controlled chambers, and core body temperature was monitored in home
956 cages placed onto a radio frequency receiver antenna (Star-Oddi, Antenna & RF-box).
957 Upon euthanasia, probes were removed and complete logged data downloaded. Core
958 body temperature was logged every 20-30 min.
959
960 **Torpor bout analysis**
961 **Classification.** To classify torpor bouts, we employed a Gaussian Mixture Model
962 in R. The classification was based on minimum body temperature and bout duration. Each
963 bout was assigned to the cluster in which it had the highest posterior probability of
964 membership. A cluster characterized by lower T_b and longer duration was designated as
965 "Deep", whereas the other cluster was classified as "Shallow". Furthermore, periods of
966 between bouts above the set T_b threshold were classified as IBE.

967 **Circadian preference.** In R, circadian preference for torpor and IBE initiation was
968 quantified using the Raleigh test of circular uniformity.
969 **Exponential decay.** In R, elapsed time in torpor for each body temperature
970 reading from torpor bouts classified as deep were determined for the first 30 hours. Next,
971 using the mean of temperatures at each time across animals, a nonlinear model was fit
972 to the data using the minimum temperature within the 30-hour period as a fixed asymptotic
973 value.
974
975 **Viral constructs**
976 AAV8-hSyn-hM4D(Gi)-mCherry (Addgene, 50475-AAV8) was obtained from
977 Addgene. AAV8-Samd3E-dTomato-nlsdTomato, AAV8-Samd3E-hM4D(Gi)-P2A-
978 nlsGFP, AAV8-Samd3E-EGFP-P2A-Synaptophysin-mRuby, and AAV8-Samd3E-
979 hM3D(Gq)-P2A-nlsGFP were produced in-house using the method previously described
980 (77) and titered via digital PCR (QIAGEN, QIAcuity). All viruses were diluted with PBS to
981 a final titer of 1E13 vg/mL before stereotaxic delivery into the hamster brain. For mice,
982 AAV8-Samd3E-hM3D(Gq)-P2A-nlsGFP with a final titer of 5E13 vg/mL was used.
983
984 **Stereotaxic viral injection**
985 **Hamster.** Hamsters were anaesthetized with 3% isoflurane and placed in a
986 stereotaxic head frame (David Kopf Instruments, model 1900). If hamsters were actively
987 hibernating, they were aroused from hibernation and placed at 22°C the day prior to
988 surgery. An air-based injection system connected to a pulled glass needle was used to
989 infuse ~100 nL of virus bilaterally at regions of interest. Hypothalamic regions were

990 targeted by referencing the hamster stereotaxic atlas (*78*). When targeting the aPOA,
991 coordinates +1.2 mm AP, ±0.4 mm ML, -7.5mm DV were used. Hamsters were allowed
992 to recover at 22°C for a minimum of 3 days before a return to 4°C chambers. Animals
993 were afforded a recovery period of at least two weeks post-surgery prior to further
994 experimental manipulation to allow for viral expression and, if appropriate, resumption of
995 hibernation.

996 **Mouse.** Mice were anesthetized with 3% isoflurane and placed in a stereotaxic
997 head frame (RWD, Guangdong, China). A Nanoject III (Drummond Scientific, Broomall,
998 PA) system connected to a pulled glass needle was used to infuse ~100 nL of virus
999 bilaterally into the aPOA (distance from Bregma, AP: +0.6 mm, ML: ±0.4 mm, DV: -5.2
1000 mm). Mice were monitored for three days post-surgery to ensure full recovery, with a
1001 waiting period of at least two weeks to allow sufficient viral expression.

1002

1003 **Chemogenetic manipulations**

1004 **Hamster.** Clozapine dihydrochloride (Hello Bio, HB6129) was either dissolved in
1005 sterile water or PBS at a concentration of 10 mg/mL and then stored at -20°C until use.
1006 For administration via drinking water, CLZ dissolved in sterile water was diluted in drinking
1007 water at a dose of 0.1 mL/kg (1 mg/kg) in a final volume of 250 mL. Animals were
1008 maintained on CLZ water for 3-7 days. For intraperitoneal (I.P.) administration, CLZ
1009 dissolved in PBS was administered at a dose of 0.5 mL/kg (5 mg/kg). In each case when
1010 treating actively hibernating hamsters, they were aroused from hibernation the morning
1011 of each experiment and treatment was administered in the evening.

1012 **Mouse.** Mice injected with AAV8-Samd3E-hM3D(Gq)-P2A-nlsGFP were single
1013 housed and placed in a temperature-controlled chamber at 8°C for three days. After three
1014 days, mice were I.P. injected with CLZ at a dose of 5 mg/kg and surface body temperature
1015 was measured using a thermal camera (Teledyne FLIR C5, Teledyne Flir, Wilsonville,
1016 OR). Images were taken before CLZ injection, and 30 min, 60 min, 3 hours, 6 hours and
1017 24 hours after CLZ injection. Analysis of surface body temperature and representative
1018 images were generated using the Flir Ignite software (https://ignite.flir.com/).
1019

1020 **Immunofluorescence**

1021 Hamsters were deeply anesthetized with isoflurane and then euthanized by
1022 transcardial perfusion of 50 mL ice-cold 1X PBS followed by 50 mL of 4%
1023 paraformaldehyde (PFA). Brains were extracted, post-fixed overnight with 4% PFA at
1024 4°C, and then embedded in 1X PBS with 3% agarose. Brains were sliced on a vibratome
1025 into 50 μm coronal sections and stored at -20°C in cryoprotectant buffer (30% sucrose,
1026 1% polyvinyl-pyrrolidone (PVP-40), 30% ethylene glycol, in 0.1 M phosphate buffer).
1027 Free-floating coronal sections were washed three times with 1X PBS and then blocked
1028 for 1 hour at room temperature with 1X PBS containing 10% donkey serum and 0.3%
1029 Triton X-100. Sections were incubated overnight at 4°C with primary antibodies (Rabbit
1030 anti-FOS, Synaptic Systems, 226-008; Rabbit anti-RFP, Rockland, 600-401-379; Chicken
1031 anti-GFP, Aves Labs, GFP-1020) diluted in 1X PBS containing 5% donkey serum and
1032 0.3% Triton X-100, washed again three times with 1X PBS, and incubated for 2 hours at
1033 room temperature with secondary antibodies in 1X PBS containing 5% donkey serum and
1034 0.3% Triton X-100. After washing three times in 1X PBS, samples were counter-stained

1035 for 15 minutes at room temperature with 1 µg/mL DAPI, washed again three times in 1X
1036 PBS, and then mounted onto SuperFrost Plus glass slides and coverslipped using
1037 Fluoromount-G.
1038
1039 **Determining deep torpor-active brain regions**
1040 Brains were collected in torpor, IBE, and from non-hibernating control animals and
1041 were processed as indicated in the section 'Immunofluorescence' using the following
1042 reagent for the detection of FOS: Rabbit anti-FOS, Synaptic Systems, 226-008.
1043 **Sample imaging.** Sections were imaged with a TissueFAXS SL whole-slide
1044 scanning system equipped with a Zeiss Axio Imager Z2 fluorescence microscope and
1045 TissueFAXS image acquisition software (Ragon Institute Microscopy Core).
1046 **Image analysis**. Using TissueQuest analysis software (TissueGnostics GmbH,
1047 Vienna, Austria), brain regions were manually annotated and nuclear DAPI signal
1048 segmented. Segmented cells containing putative FOS signal were determined to be FOS-
1049 positive based on diameter and mean fluorescence intensity. In R, regional cell counts
1050 were analyzed and percent active neurons determined by the fraction of FOS-positive
1051 and total DAPI-positive cells. Significance was calculated using a mixed-effects ANOVA
1052 with post-hoc pairwise comparisons. Pairwise comparison p-values were multiple tests
1053 corrected using the Bonferonni method.
1054
1055 **Mapping of virally injected hypothalamic nuclei and correlation with**
1056 **chemogenetically induced torpor perturbation**

1057 Hibernating hamsters were bilaterally injected with AAV8-hSyn-hM4D(Gi)-
1058 mCherry. Upon resumption of hibernation, hamsters were administered CLZ water for ~3
1059 days (74 hours) to inhibit virally injected regions, and their core body temperature were
1060 recorded.

1061 **Temperature data analysis.** Upon CLZ water treatment, hamsters reinitiating
1062 deep torpor within 48 hours were classified as unperturbed, and those failing to reinitiate
1063 (remaining euthermic) within this time were classified as perturbed. Sham surgery control
1064 animals treated with CLZ water for 7 days informed this threshold (**Fig. S2C**). Absolute
1065 elapsed time of euthermia from start of treatment was used for further analysis.

1066 **Sample imaging.** Given the unavoidable variability in hypothalamic region
1067 targeting and viral spread, all hamsters were euthanized for post hoc assessment of
1068 transduced brain regions. Collected brains were processed as indicated in the section
1069 'Immunofluorescence' to detect endogenous mCherry fluorescence. Sections were
1070 imaged with a TissueFAXS SL whole-slide scanning system equipped with a Zeiss Axio
1071 Imager Z2 fluorescence microscope and TissueFAXS image acquisition software (Ragon
1072 Institute Microscopy Core).

1073 **Image and correlation analysis.** Viral mCherry expression was quantified across
1074 70 hypothalamic regions in a semi quantitative manner, where the viral expression was
1075 scored 0 (none), 1 (minimal), 2 (partial), or 3 (complete) in each region and hemisphere.
1076 The analysis was performed blinded to whether perturbation of torpor was observed in
1077 each hamster. To assign a single numeric value for each hypothalamic region in each
1078 hamster, we added the semiquantitative expression values from each hemisphere. Next,

1079 a Pearson correlation was calculated for each region across all hamsters between the
1080 viral expression in that region and the length of time spent euthermic.
1081
1082 **Nuclei dissociation and single-cell analysis**
1083 Preoptic area tissue was dissected from adult male and female Syrian hamsters
1084 and immediately flash-frozen. The 10X genomics nuclei isolation kit (1000448) was used
1085 to obtain dissociated nuclei. Tissue was homogenized on ice in a detergent-based nuclei
1086 isolation buffer, passed through a 40-µm filter, and purified by centrifugation. Nuclei were
1087 washed, and counted before loading. Single-nucleus multiome libraries were prepared
1088 using the 10x Genomics Chromium Single Cell Multiome ATAC + Gene Expression
1089 workflow following the manufacturer's protocol. Constructed libraries were quantified,
1090 pooled, and sequenced on an Illumina platform to recommended depth for both
1091 modalities. The raw data were processed in parallel with cellranger-arc to generate gene-
1092 expression count matrices, ATAC fragment files, and peak-by-cell accessibility matrices.
1093 A recently published mouse POA multiome dataset generated with the same 10x system
1094 was obtained to build a reference dataset. A combination of scVI and Scanpy (*79*, *80*)
1095 pipelines were used to process and integrate the two datasets, including quality control
1096 (filtering by gene counts, UMI counts, and mitochondrial RNA content), normalization, log-
1097 transformation, identification of highly variable genes, dimensionality reduction,
1098 neighborhood graph construction, and Leiden clustering.
1099 To ensure that downstream analyses focused on POA-associated neuronal
1100 populations, we used the MERFISH dataset as a spatial reference (*61*). To this end,
1101 mouse spatial transcriptomic data was subset to only include neurons found in the mPOA

1102 and co-clustered with mouse neuronal snRNA-seq. Canonical POA markers and spatial
1103 annotations were used to confirm that the identified clusters in both species corresponded
1104 to POA-localized neuronal subtypes. Subsequently, the reference mouse dataset was
1105 used to identify homologous hamster neurons through integration and label transferring
1106 with scANVI (*81*). Chromatin accessibility matrices were analyzed with Pycistopic (*82*)
1107 including psuedobulking, peak calling and filtering, identification of co-accessible regions
1108 and differential accessibility analysis.
1109

1110 **Double fluorescent *in situ* hybridization and immunofluorescence**

1111 Hamsters were deeply anesthetized with isoflurane and then euthanized by
1112 transcardial perfusion of 50 mL ice-cold 1X PBS followed by 50 mL of 4% PFA. Brains
1113 were extracted, post-fixed overnight with 4% PFA at 4°C, and then incubated in 1X PBS
1114 with 30% sucrose at 4°C until fully infiltrated and sunk to the bottom of the chamber (72-
1115 96 hours). Brains were embedded in Optimal Cutting Temperature (O.C.T.) compound,
1116 frozen on dry ice, and stored at -80°C until use. Brains were sliced on a cryostat (Leica
1117 CM3050 S) into 10-30 μm coronal sections, placed in cryoprotectant buffer, and stored at
1118 −20°C until use. Free-floating coronal sections were washed three times with 1X PBS,
1119 mounted onto Superfrost Plus slides, and then baked for 45 minutes at 60°C. Subsequent
1120 steps followed the standard fluorescent *in situ* hybridization protocol for the RNAscope
1121 Fluorescent Multiplex V2 Assay using the following probes: Mau-*Samd3*-C1 (1826261),
1122 Mau-*Slc17a6*-C2 (1176381), Mau-*Adcyap1*-O1-C3 (1808861), Mau-*Slc32a1*-C4
1123 (1176381).

1124 Upon completion of *in situ* hybridization, samples immediately were processed
1125 according to the ACD RNAscope Fluorescent Multiplex V2 Assay Combined with
1126 Immunofluorescence manual with the following modifications: Slide-mounted sections
1127 were washed twice in 1X TBS with 0.005% Tween-20 (TBST), blocked for 1 hour at room
1128 temperature with 1X TBS containing 10% donkey serum, and incubated overnight at 4°C
1129 with primary antibodies (Rabbit anti-FOS, Synaptic Systems, 226-008; Rabbit anti-RFP,
1130 Rockland, 600-401-379; Chicken anti-GFP, Aves Labs, GFP-1020) diluted in 1X TBS
1131 containing 5% donkey serum. Slides were washed three times with TBST, incubated for
1132 2 hours at room temperature with secondary antibodies in 1X TBS containing 5% donkey
1133 serum, washed again three times with TBST, counter-stained for 15 minutes at room
1134 temperature with 1 µg/mL DAPI, washed three times with 1X TBS, and finally mounted
1135 on coverslips using ProLong Gold.

1136 **Sample imaging.** Sections were either imaged with a TissueFAXS SL whole-slide
1137 scanning system equipped with a Zeiss Axio Imager Z2 fluorescence microscope and
1138 TissueFAXS image acquisition software (Koch Institute Swanson Biotechnology
1139 Center/Microscopy Core) or a Leica Stellaris 8 FALCON confocal microscope (Whitehead
1140 Institute W.M. Keck Facility for Biological Imaging).

1141 **Image analysis**. Using QuPath software(*83*), colocalization analysis of RNAscope
1142 and immunofluorescent signals was performed. After manual annotation of regions of
1143 interest, the InstanSeg extension (*84*) was utilized for cell segmentation, considering each
1144 fluorescent signal. Next, segmented cells containing putative RNAscope and
1145 immunofluorescent signals were determined to be positive or negative for associated
1146 markers based on diameter and mean fluorescence intensity. Subsequent quantification

1147 of counts was performed in R, while plotting and statistical analysis was performed in
1148 GraphPad Prism software (Boston, MA).
1149
1150 **Inhibition of aPOA^{Vglut2} neurons**
1151 Hibernating hamsters were bilaterally injected with either AAV8-Samd3E-
1152 hM4D(Gi)-P2A-nlsGFP or AAV8-Samd3E-EGFP-P2A-Synaptophysin-mRuby. On the
1153 day of treatment, hamsters were aroused in the morning, I.P. injected with CLZ and
1154 provided with CLZ water in the evening, I.P. injected again 16 hours later, and core body
1155 temperature recorded. This regimen accounted for variability in water intake within the
1156 first 24 hours of the experiment and maximized inhibition of our targeted population. A
1157 CLZ water treatment window of 6 days (144 hours) was used. For PBS control treatment,
1158 an identical regimen was followed.
1159 **Temperature data analysis.** In GraphPad Prism (Boston, MA), absolute elapsed
1160 time of euthermia from start of treatment was used to determine differences within groups.
1161 The treatment window duration (144 hours) was applied as an upper bound for statistical
1162 analysis. In R, temperature data from each virus group and treatment condition was
1163 mapped to circadian time. In GraphPad Prism (Boston, MA), statistical analysis was
1164 performed on temperatures in the light and dark cycles within virus groups.
1165
1166 **Excitation of aPOA^{Vglut2} neurons**
1167 Hamsters were bilaterally injected with either AAV8-Samd3E-hM3D(Gq)-P2A-
1168 nlsGFP or AAV8-Samd3E-EGFP-P2A-Synaptophysin-mRuby and housed at 4°C to
1169 acclimate. On the day of treatment, hamsters were aroused in the morning, I.P. injected

1170 with CLZ in the evening, and core body temperature recorded. For PBS control treatment,
1171 an identical regimen was followed.

1172 **Temperature data analysis.** In R, temperature data was analyzed using the
1173 method described in section 'Torpor bout analysis' to determine if the CLZ induced drop
1174 in body temperature clustered with either deep or shallow torpor. In GraphPad Prism
1175 (Boston, MA), statistical analysis was performed on minimum temperatures across each
1176 condition (euthermia, torpor, CLZ, and PBS).

1177 **Sample imaging.** Collected brains were processed as indicated in the section
1178 'Immunofluorescence' using the following reagent for the detection of AAV8-Samd3E-
1179 hM3D(Gq)-P2A-nlsGFP: Chicken anti-GFP, Aves Labs, GFP-1020. Sections were
1180 imaged with a TissueFAXS SL whole-slide scanning system equipped with a Zeiss Axio
1181 Imager Z2 fluorescence microscope and TissueFAXS image acquisition software (Koch
1182 Institute Swanson Biotechnology Center/Microscopy Core).

1183 **Image and correlation analysis.** aPOA GFP expression was quantified in a semi
1184 quantitative manner where expression was scored 0 (none), 1 (minimal), 2 (partial), or 3
1185 (complete) in each hemisphere. The analysis was performed blinded to change in body
1186 temperature observed in each hamster. Hemispheric values were summed within
1187 animals. In GraphPad Prism (Boston, MA), a Pearson correlation was performed between
1188 GFP viral expression and the minimum body temperature.

1189

1190 **Behavioral analysis**

1191 Hamsters housed at 4°C and injected with AAV8-Samd3E-hM3D(Gq)-P2A-
1192 nlsGFP or AAV8-Samd3E-EGFP-P2A-Synaptophysin-mRuby were I.P. injected with PBS

1193 (0.5 mL/kg) after a one-hour baseline video recording of homecage behavior and an
1194 additional hour recording post injection. Following at least a week recovery in 4°C
1195 chambers, animals were injected with CLZ (5 mg/kg) and videos were recorded for one
1196 hour before and post drug administration in 4°C chambers. Homecage behaviors were
1197 manually coded using BORIS software (*85*). Behavior was coded 30 min after PBS or
1198 CLZ injection over a 10 min window.